IN VIVO IMAGING OF CORTICAL POROSITY BY SYNCHROTRON PHASE CONTRAST MICRO COMPUTED TOMOGRAPHY

A Thesis Submitted to the College of

Graduate Studies and Research

In Partial Fulfillment of the Requirements

For the Degree of Masters of Science

In the Department of Anatomy and Cell Biology

University of Saskatchewan

Saskatoon

By

ISAAC PRATT

PERMISSION TO USE

In presenting this thesis in partial fulfilment of the requirements for a Postgraduate degree from the University of Saskatchewan, I agree that the Libraries of this University may make it freely available for inspection. I further agree that permission for copying of this thesis in any manner, in whole or in part, for scholarly purposes may be granted by the professor or professors who supervised my thesis work or, in their absence, by the Head of the Department or the Dean of the College in which my thesis work was done. It is understood that any copying or publication or use of this thesis or parts thereof for financial gain shall not be allowed without my written permission. It is also understood that due recognition shall be given to me and to the University of Saskatchewan in any scholarly use which may be made of any material in my thesis.

Requests for permission to copy or to make other use of material in this thesis in whole or part should be addressed to:

Head of the Department of Anatomy and Cell Biology

University of Saskatchewan

Saskatoon, Saskatchewan, S7N 5E5

ABSTRACT

Cortical bone is a dynamic tissue which undergoes adaptive and pathological changes throughout life. An improved understanding of the spatio-temporal process of remodeling holds great promise for improving our understanding of bone development, maintenance and senescence. The use of micro-computed tomography (μCT) on living animals is relatively new and allows the three dimensional quantification of change in trabecular bone microarchitecture over time. The use of *in vivo* μCT is limited by the radiation dose created by the x-ray beam, with commercially available *in vivo* systems generally operating in the 10-20 um resolution range and delivering an absorbed dose between 0.5-1 Gy. Because dose scales to the power of four with resolution, *in vivo* imaging of the cortical canal network, which requires a higher resolution, has not been achieved. I hypothesized that using synchrotron propagation phase contrast μCT, cortical porosity could be imaged *in vivo* in rats at a dose on the same level as those used currently for trabecular bone analysis. Using the BMIT-BM beamline, I determined the optimal propagation distance and used ion chamber and lithium fluoride crystal thermoluminescent dosimetry to measure the absorbed dose of my *in vivo* protocol as well as several *ex vivo* protocols using synchrotron phase contrast μCT at 5 μm, 10 μm, and 11.8 μm and conventional desktop *in vivo* protocols using commercial μCT systems. Using synchrotron propagation phase contrast μCT, I scanned the forelimb of two adult Sprague-Dawley rats and measured an absorbed dose of 2.53 Gy. Using two commercial μCT system, I measured doses between 1.2-3.6 Gy for protocols at 18μm that are in common use. This thesis represents the first *in vivo* imaging of rat cortical porosity and demonstrates that an 11.8 μm resolution is enough to visualize cortical porosity in rats, with a dose within the scope of those used for imaging trabecular bone *in vivo*.

ACKNOWLEDGEMENTS

I am grateful for the contributions and efforts of many colleagues and friends that have made this thesis possible. To begin, I must thank my supervisor Dr. David Cooper, for taking a chance on me. His expertise, knowledge, and patience has made my graduate experience profound and worthwhile. The rest of my graduate committee, Dr. Julia Boughner and Dr. Dean Chapman, deserve many thanks as well, for critical but kind words and assistance freely given.

I have had the great fortune to encounter many great academics though the start of my academic career, and they have been inspirations and goals. I've learned more from you than you know. In no particular order, Dr. Susan Pfeiffer, Dr. Emmanuel Istrate, Dr. David Begun, Dr. Bonnie Glencross, Dr. Gerry De Iuliis, Dr. Ernie Walker, Dr. Angela Lieverse, and Dr. Gregg Adams.

To everyone who contributed to the development of this thesis, thank you. Dr. George Belev, your support at BMIT has been invaluable. Without you and the rest of the BMIT team, Dr. Tomasz Wysokinski, Dr. Adam Webb, and Dr. Ning Zhu, I'd be lost in a sea of murk and radiation. To Dr. Mike Doschak and Imran Khan in Alberta, your assistance was indispensable.

To my friends in the lab, the department, and at the University, thank you. Yasmin Carter, Kim Harrison, Cheryl Hennig, Treena Swanston, Carter Britz, Mylyne Tham, Megan Clarke, Muhammad Raj, without you all I'd surely have gone mad.

To my family, without your support, I would not have made it here. Mom and Dad, thank you for believing in me, and supporting me through all my ups and downs, and encouraging me in all my strange interests. To my brother, thanks for putting up with me.

To my friends, in Saskatoon and in Toronto, and elsewhere. Thank you for being there. To Averi and Millie, you made Saskatchewan easier. To KAKC, VL, SR, BO, HK, MEC, SLD, JN, SC, AA, JS, you make my life better by being in it.

To everyone mentioned and not mentioned, there aren't enough terms in the thesaurus to properly thank you.

To my rats, thank you for your sacrifice.

For my parents, if you think this is long, just wait till you see the next one

TABLE OF CONTENTS

PERMISSION TO USE i
ABSTRACT ii
ACKNOWLEDGEMENTS iii
DEDICATION v
TABLE OF CONTENTS vi
LIST OF TABLES viii
LIST OF FIGURES ix
LIST OF ABREVIATIONS xii
CHAPTER ONE: INTRODUCTION 1
1.1 Introduction 1
1.2 Bone microstructure 1
1.3 Bone growth and repair 3
1.3.1 Growth 3
1.3.2 Modeling 3
1.3.3 Remodelling 3
1.4 Cortical bone imaging 6
1.5 Organization of the thesis 8
CHAPTER 2: THE STATE OF *IN VIVO* MICRO-COMPUTED TOMOGRAPHY IMAGING OF BONE 9
2.1 Introduction to bone microstructure 9
2.1.1 Trabecular bone 9
2.1.2 Cortical bone 13
2.2. Micro computed tomography 16
2.2.1 Synchrotron µCT 16
2.2.2 Desktop µCT 17
2.2.3 Dose 17
2.2.4 Dosimetry 19
2.2.5 Scan parameters impacting dose 21
2.3 Small animal µCT *in vivo* 23
2.3.1 Synchrotron in vivo µCT 25
2.3.2 Desktop in vivo µCT 27
2.3.3 Effects of radiation dose on bone 29
2.4 Conclusion 34
CHAPTER 3: PHASE CONTRAST SYNCHROTRON µCT 35
3.1 Introduction 35
3.2 Phase contrast 36
3.3 Materials and methods 43
3.3.1 Animals 43
3.3.2 Synchrotron ex vivo µCT 43
3.3.3 Ex vivo phase contrast setup and optimization 45
3.3.5 Synchrotron in vivo µCT 45

3.3.4 Desktop μCT 47
3.3.6 Software 49
3.3.7 Dosimetry 49
3.4 Results 50
3.4.1 Resolution 50
3.4.2 Impact of number of projections 51
3.4.2 Propagation distance 52
3.4.3 Energy differences 53
3.4.4 dosimetry 54
3.4.5 in vivo SR μCT 55
3.4.6 Comparison with desktop μCT 57
3.5 Discussion 60
3.6 Conclusions 64
CHAPTER FOUR: CONCLUSION 66
4.1 Overview 66
4.2 Future Directions 67
4.3 Conclusion 70
REFERENCES 71

LIST OF TABLES

Table 2.1: Definition and description of 3D trabecular bone quantification parameters..... 11

Table 2.2: Definition and description of 3D cortical bone gross geometrical and microstructural quantification parameters..... 15

Table 2.3: Synchrotron protocols and their major features..... 32

Table 2.4: Desktop μCT protocols and their major features..... 33

Table 3.1: Synchrotron μCT imaging protocols used..... 46

Table 3.2: Desktop μCT imaging protocols..... 49

Table 3.3: Measured doses for the different protocols..... 55

LIST OF FIGURES

Figure 1.1: Cortical bone. On the left of (A), a segment of a cross-section of human metacarpal cortical bone, surround the marrow cavity on the right of (A). In (B), a 3D volume render of a μCT cross-section of the same bone. In (C), a render of a segment of the neurovascular canal network. 2

Figure 1.2: Trabecular bone. A 3D volume render of trabecular bone from the proximal radius of a rat 2

Figure 1.3: The basic structure of a BMU, with the osteoclast cutting cone shown at 'A', the resorption space shown at 'B', the osteoblast closing cone at 'C', and the resulting lamellar bone surrounding a Haversian canal at 'D'..... 4

Figure 2.1: Illustration of the MIL method of DA calculation. The mean intercept length is found by passing a line through a 3D volume containing the region of interest, counting the number of intersections this line makes with part of the tissue (in this case bone) in the region of interest, and dividing this number by the length of the line. Differences in the MIL across different angles reflect the anisotropy in the bone. As seen in 'A', lines passing through the sample intercept the bone a different number of times depending on their orientation with respect to the anisotropy of the tissue. In 3D, many such lines are passed through the tissue ('B') to obtain MILs for a large number of angles to fully quantify the anisotropy over the whole volume. Next each line is drawn passing through the origin ('C'), and the resulting polar plot is fitted to a 3D ellipsoid with three main axes. The ellipsoid can be described as a tensor (3D matrix) with eigenvectors describing the strength of the anisotropy in the three major directions. From this tensor the DA can be calculated, by subtracting the division the maximum eigenvalue by the minimum eigenvalue from 1. The DA can then range from 0 to 1, where 0 is total isotropy and 1 is total anisotropy. Figure adapted from the CT-analyser manual (Bruker 2012). 12

Figure 2.2: The energy absorption coefficients for soft tissue (ICRU4 NIST standard) and solid bone (NIST) in cm^2/g plotted against energy, showing the decrease in energy absorption, and therefore absorbed dose, with higher x-ray energy. (Data from NIST, http://www.nist.gov/) 23

Figure 3.1: Phase contrast imaging setups. In A, the setup for propagation phase contrast is shown, with the increased sample-detector distance. In B, the setup for DEI is shown, with the analyzer crystal. In C, the setup for grating based phase contrast is shown, with the source grating G0, the phase grating G1, and the analyzer grating G2. 39

Figure 3.2: Changes in the x-ray waveform through the use of propagation phase contrast..... 40

Figure 3.3: The edge-enhancement effect can be seen in the graph on the right, where the bone tissue is on the left and the background is on the right. The phase peak has gray levels higher than the bone and lower than the background. The area in the graph is shown as the yellow line in the synchrotron μCT slice on the left..... 41

Figure 3.4: The x-ray source brightness for the BMIT bending magnet beam line, from 0 to 100 keV. 44

Figure 3.5: Rats positioned in the custom stage built at BMIT. On the left, a variant with the arm positioned in a tube in the beam. On the right, a variant with the arm held in a tube by a bridge. 46

Figure 3.6: The difference between resolutions with 5 µm and 10 µm voxels using the C4742-98-ERG camera. The phase propagation distance for the 5 µm image is 0.3 m and for the 10 µm image is 0.6 m. 51

Figure 3.7: The impact of the number of projections on image quality can be seen, with a scan of 360 projections on the left compared to a scan of 750 projections on the right. These scans were performed with the C4742-98-ERG camera at 10 µm, and all other parameters were kept equal. Slice matches are not exact. 52

Figure 3.8: The optimal phase distance for the C4742-98-ERG camera at 10 µm was found to be 0.6 m. Selected propagation distances of 0.1 m, 0.6 m, and 1.0 m are shown for comparison. 52

Figure 3.9: The optimal phase distance for the C4742-98-ERG camera at 5 µm was found to be 0.3 m. Selected propagation distances of 0.1 m, 0.6 m, and 0.6 m are shown for comparison. Slice matches are not exact. 53

Figure 3.10: The optimal phase distance for the C4742-56-12HR camera was found to be 0.9 m. Selected propagation distances of 0.25 m, and 0.9 m are shown for comparison. Slice matches are not exact. 53

Figure 3.11: Differences in image quality using different x-ray energy in the tibia imaged using the C4742-98-ERG camera at 10 µm using a propagation distance of 0.6 m. Slice matches are not exact. 54

Figure 3.12: Single slice from the *in vivo* synchrotron µCT showing cortical porosity measured using the C4742-56-12HR camera at 11.8 µm with a 2.53 Gy dose. 56

Figure 3.13: Longitudinal slice parallel to the long axis of the forelimb shows canals within the cortical bone, resliced in ImageJ from the *in vivo* scan using the C4742-56-12HR camera at 11.8 µm. 56

Figure 3.14: Volume render of the cortical porosity in the forelimb µCT scan 57

Figure 3:15: Slice reconstructed from the *in vivo* desktop SkyScan 1076 at 35 µm. Matching slice to the Synchrotron *in vivo*, any deviation is from positioning differences during the scans. Dose was not measured but is presumed to be lower than other scans. 58

Figure 3:16: Slice reconstructed from the *in vivo* desktop SkyScan 1176 at 18 µm with a 1.2-1.5 Gy dose. Matching slice to the Synchrotron *in vivo*, any deviation is from positioning differences during the scans. 58

Figure 3:17: Slice reconstructed from the *in vivo* desktop SkyScan 1176 at 9 µm with an 11.7-18.2 Gy dose. Matching slice to the Synchrotron *in vivo*, any deviation is from positioning differences during the scans. 59

Figure 3.18: Slice reconstructed from the *ex vivo* desktop SkyScan 1172 at 6.5 µm. Matching slice to the Synchrotron *in vivo*, any deviation is from positioning differences during the scans. Dose was not measured but is presumed to be higher than other scans. 59

Figure 3.19: Brightness of the BMIT insertion device beamline compared to the BMIT bending magnet beamline. 63

LIST OF ABREVIATIONS

° = degrees
2D = two dimensional
3D = three dimensional
BMU = basic multicellular unit
BMIT = BioMedical Imaging and Therapy
BM = bending magnet
CT = computed tomography
DEI = diffraction enhanced imaging
Gy = gray
ID = insertion device
keV = kiloelectronvolt
kV = kilovolt
mA = milliampere
mGy = milligray
mm = millimeter
OSL = optically stimulated luminescence
OVX = ovariectomized
ROI = region of interest
SR = synchrotron radiation
TLD = thermoluminescent dosimeter
vs = versus
µA = microampere
µCT = micro-computed tomography
µm = micron

CHAPTER ONE: INTRODUCTION

1.1 Introduction

Bone is a complex, dynamic tissue found in most living vertebrates, constantly adapting in response to internal and external stimuli. The only current living vertebrates without bone are the 'cartilaginous fishes', modern chondrichthyans such as sharks, rays, and skates, and even these animals are likely to have evolved from ancestral vertebrates containing bone (Eames et al. 2007). Bone forms a rigid endoskeleton for an animal and provides many important functions in the body including red and white blood cell production in the marrow, and storage for minerals, heavy metals, and alkaline salts (Currey 2002). Approximately 65% of the dry weight of a bone is made up of a calcium-phosphate mineral, hydroxyapatite, which provides the majority of a bone's compressive strength. The remaining 35% is organic, and mostly composed of collagen fibers along with a small percentage of other proteins (Pearson and Lieberman 2004), which is responsible for the bones tensile strength.

1.2 Bone microstructure

Bone has two main tissue types: cortical bone and trabecular bone. The first, illustrated in figure 1, is an outer, dense shell of bone with a perforating network of neurovascular canals, which surrounds the marrow cavity and in long bones is concentrated mainly in the diaphysis. The second, illustrated in figure 2, is trabecular bone, an inner load bearing compartment forming a mesh-like network of struts and plates, which in long bones is found mainly in the epiphyses (Currey 2002). These two bone tissues play different roles, complementing each other and working together to create a whole that is stronger than the sum of its parts.

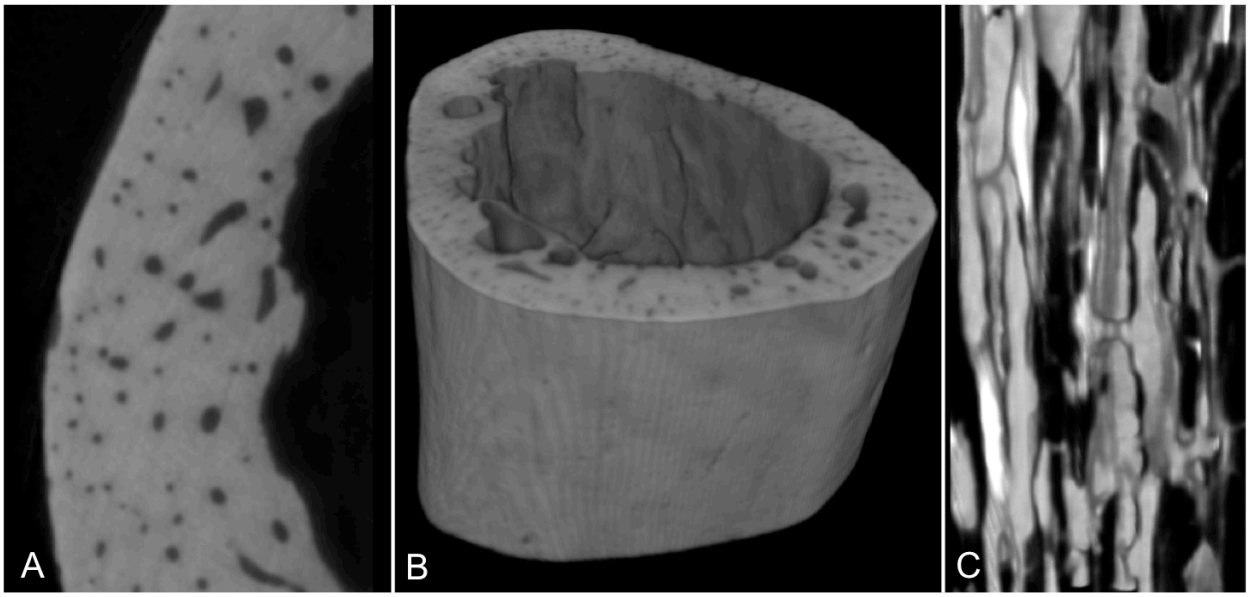

Figure 1.1: Cortical bone. On the left of (A), a segment of a cross-section of human metacarpal cortical bone, surround the marrow cavity on the right of (A). In (B), a 3D volume render of a μCT cross-section of the same bone. In (C), a render of a segment of the neurovascular canal network.

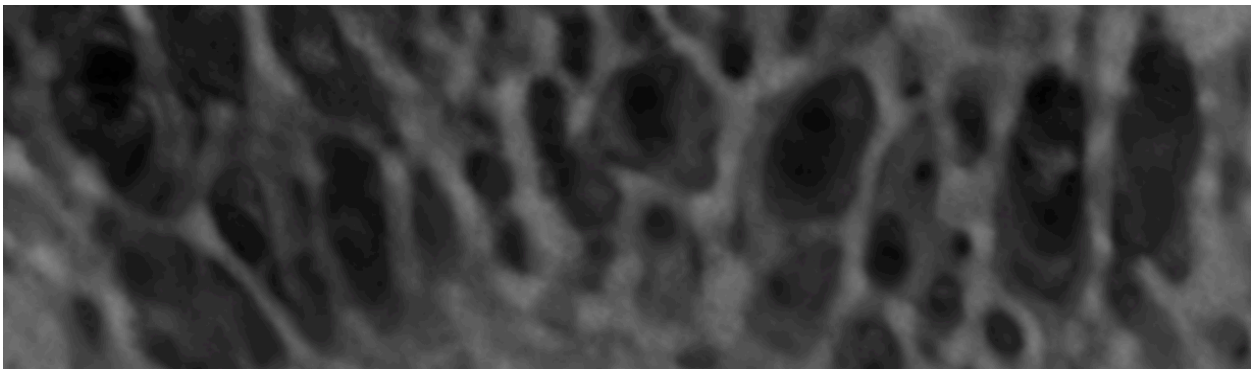

Figure 1.2: Trabecular bone. A 3D volume render of trabecular bone from the proximal radius of a rat

1.3 Bone growth and repair

1.3.1 Growth

Both trabecular and cortical bone undergo similar types of adaptation and renewal throughout life; this thesis will focus primarily on the aspects of bone growth and development that relate to cortical bone. The processes through which bone growth and development occur can be grouped into three main categories: longitudinal growth, modeling and remodelling (Frost 1987). The longitudinal growth of bone is simply the addition of new primary trabeculae and cortical length to a bone over time.

1.3.2 Modeling

Modeling changes the geometry of the bone, including its shape and size, and takes place predominantly during the initial growth of the bone. As a result, bone formed during modeling is called primary bone. Primary bone is laid down quickly, encompassing neurovascular canals in the bone and forming primary osteons (Cooper et al. 2004). Primary bone can be laid down either as woven bone, with irregularly oriented collagen fibres, or as lamellar bone, in concentric layers forming circumferential rings in the diaphysis (Currey 2002).

1.3.3 Remodelling

Over an animal's lifespan, this initially formed bone can be removed and replaced through remodelling. This process, which is dominant in larger terrestrial vertebrates, plays either only a minor role in bone upkeep or is absent in smaller animals such as mice and rats. Remodelling proceeds through the coordinated action of collections of bone cells working together as a Basic Multicellular Unit (BMU). Initiation of a BMU occurs with osteoclasts forming a cutting cone to remove existing bone, forming a resorption space, which is then filled in with osteoid, and mineralized by osteoblasts in a closing cone. A new canal is formed around

the neurovascular support for the cells, surrounded by concentric rings of new bone called lamellae (Robling et al. 2006). See figure 3 for details. The result of such remodelling is the continual creation of new vascular canals in the tissue.

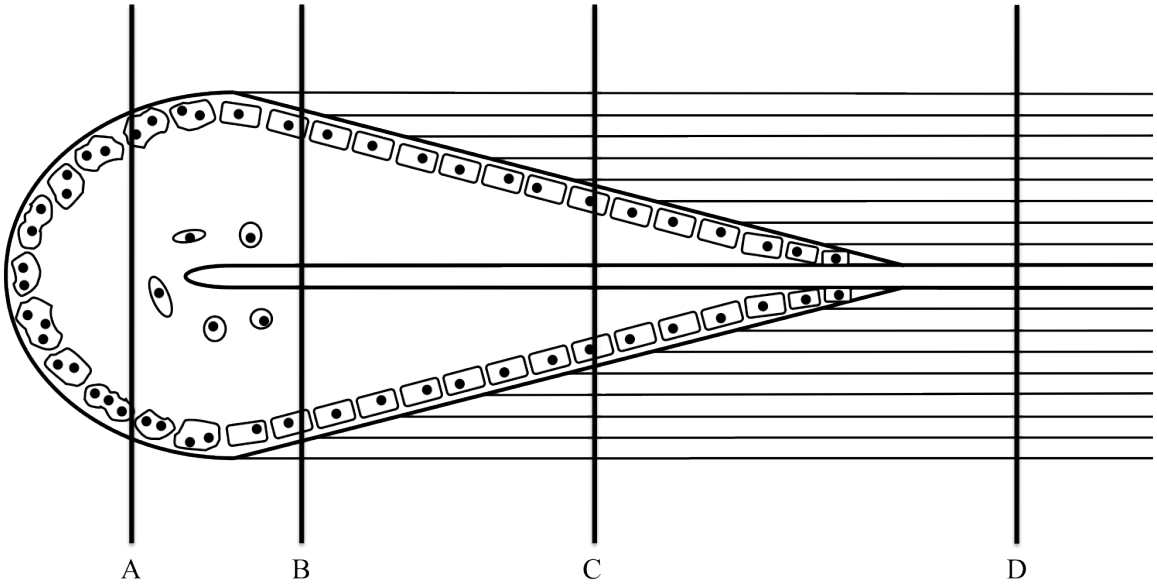

Figure 1.3: The basic structure of a BMU, with the osteoclast cutting cone shown at 'A', the resorption space shown at 'B', the osteoblast closing cone at 'C', and the resulting lamellar bone surrounding a Haversian canal at 'D'.

These canals and the surrounding lamellae are known as Haversian systems or secondary osteons (Frost 1963). This process of remodelling has a significant impact of the strength of bone and its adaptation (Ammann and Rizzoli 2003). While trabecular bone orientation has long been used to infer loading environments (Koch 1917; Ryan and Shaw 2012), research investigating the relationships between canal structure and loading has been a more recent development (Britz et al. 2012b; de Margerie 2002). The orientation of the canals within both primary and secondary bone responds to the mechanical loading environment during their formation, similar to how the trabecular bone mesh responds to those same forces. Therefore, primary canals are likely to reflect conditions during growth while secondary canals and BMUs reflect loading conditions

over the course of the remodelling processes. Specifically, BMU orientation has been shown to align with the predominant stress orientation experienced by a bone (Hert et al. 1994; Petrtyl et al. 1996), indicating that the osteoclasts in the BMUs are sensing a stress or strain related signal.

These signals are produced by osteocytes embedded in the bone, which sense mechanical stimuli and fluid flow in the lacunar-canalicular network (LCN) (Weinbaum et al. 1994) and translate them by mechanotransduction into electrochemical signals which can be acted on by neighbouring cells including osteoclasts and osteoblasts (Duncan and Turner 1995). Burger et al. (2003), showed that in the absence of fluid shear stress osteocytes underwent apoptosis and hypothesized that these apoptotic osteocytes attracted nearby osteoclasts. This would direct the progression of the cutting cone of BMUs locally, while the general course of their travel through the bone would be directed by changes in LCN interstitial fluid pressure aligned with the primary orientation of stress on the bone. Remodelling is at least partially initiated by microdamage caused by mechanical fatigue loading (Burr et al. 1985), where microcracks produced by cyclic loading are diverted into the lamellar structure of osteons. Martin proposed that all remodelling in normal tissue was induced by such microdamage (Martin 2002) and that BMUs can be initiated by this and steered towards the resultant microcracks, which have caused the death of nearby osteocytes (Martin 2007). The effect of this would be to remodel the bone containing the microcrack and repair the damage.

The importance of the remodelling process can be easily noted as osteoporosis may result from a deficiency in the mechanotransduction system, whereby the bone would lose its ability to respond to loading (Santos et al. 2009; Seeman 2004). An imbalance in the remodelling process, an increase in osteoclastic resorption activity or a decrease in the formation of new bone by osteoblasts, can lead to decreased bone mass and density, and ultimately osteoporosis (Eriksen

2010). The ability to study the development of cortical porosity directly is therefore key to elucidating the nature of remodelling, and in particular the ability to longitudinally image *in vivo* and track the development and progression of BMUs in bone has the potential to answer many questions related to remodelling processes.

1.4 Cortical bone imaging

Imaging cortical bone has traditionally been done using dry bone histological methods (Frost 1958), which while providing a wealth of knowledge are fundamentally limited as they cannot yield a full understanding of the three-dimensional (3D) nature of the bone microstructure. In response to this, serial sectioning histological techniques were developed which provide some three dimensional information (Dehoff 1983; Odgaard et al. 1990; Parfitt et al. 1987); however, such methods can be tedious and require destruction of the specimens under study. As a result such methods have largely been superseded by the use of micro-computed tomography (μCT). μCT was first used for the 3D imaging of bone microstructure in 1989 (Feldkamp et al. 1989) and has several key advantages, including the ability to do quantitative 3D analysis of the resulting digital image data of the microstructure, as well as preservation of the specimen. Many studies have since used desktop μCT to image the cortical network in humans (Basillais et al. 2007; Borah et al. 2010; Chen et al. 2010; Cooper et al. 2006; Cooper et al. 2007b; Cooper et al. 2003; Particelli et al. 2012; Wachter et al. 2001) and in rats (Britz et al. 2010; Britz et al. 2012b; Jast and Jasiuk 2013). Desktop μCT has also been used to study trabecular dynamics *in vivo* in small animals such as mice and rats (Boyd et al. 2006a; Brouwers et al. 2007; Klinck et al. 2008; Matsumoto et al. 2011; Waarsing et al. 2004a).

μCT studies have also commonly used synchrotron x-ray sources as they can provide several advantages over desktop sources leading to greater quality images. These include higher

resolution and greater x-ray flux leading to the capacity for a monochromatic beam (Schneider et al. 2007). Synchrotron μCT (SRμCT) is the current gold standard for imaging bone microstructure and its advantages have been applied to both cortical bone and trabecular bone imaging (Matsumoto et al. 2011; Matsumoto et al. 2006; Matsumoto et al. 2007). SRμCT also provides the ability to use alternate contrast mechanisms such as phase contrast to illuminate bone features (Zhou and Brahme 2008).

The progression of *in vivo* μCT to higher resolution has been limited by the corresponding increase in radiation dose, where an increase in resolution by a factor of two while maintaining equivalent image quality increases the dose by a factor of sixteen (Ford et al. 2003). Desktop μCT is able to image trabecular bone microarchitecture at a safe level around 1 Gy and under in small animals such as mice or rats. However, at higher resolutions these doses become intolerable to the animals welfare, and effects can be seen in the bone tissue. As a result, *in vivo* imaging of cortical bone has as yet been unachieved. The primary goal of this thesis was to test the hypothesis that synchrotron phase contrast micro-CT is capable of resolving cortical bone porosity *in vivo* with a safe radiation dose. Specifically, the objective was the development of a protocol allowing the visualization of cortical neurovascular porosity in living rats at a dose comparable to that imparted by desktop imaging systems utilized for trabecular bone imaging. Since desktop μCT systems do not have the flexibility of techniques available that are achievable at a synchrotron, this objective was achieved through the use of phase contrast SRμCT at the Canadian Light Source synchrotron. The ability to perform longitudinal studies tracking cortical porosity progression will allow direct testing of causative hypotheses relating to remodelling and connected disease processes.

1.5 Organization of the thesis

Chapter 2 provides a review of the current state of μCT imaging, touching on both desktop and synchrotron sources, focusing specifically on *in vivo* bone imaging and imaging protocols as well as their specific limitations, primarily with regards to the radiation dose involved. This chapter will explore the quantitative parameters used to describe trabecular and cortical bone, the nature of radiation dose, the factors involved in dose, and examine the doses created by *in vivo* μCT protocols, the effects of these doses, and the methodology used to measure them.

Chapter 3 starts with a recap of cortical bone remodelling and an examination of x-ray propagation phase contrast imaging methods. It then describes the development of the protocol which is the focus of this thesis, the use of phase contrast SRμCT to visualize and quantify the cortical architecture of living small animals. Starting with *ex vivo* tissues, a series of SRμCT feasibility tests were performed, including phase distance determination and optimization. This experiment culminated with a terminal *in vivo* study which was able to visualize cortical porosity at a measured dose of 2.53 Gy.

Chapter 4 discusses the results, concludes the thesis, positions the main findings in relation to the current state of bone μCT research and discusses future research directions.

CHAPTER 2: THE STATE OF *IN VIVO* MICRO-COMPUTED TOMOGRAPHY IMAGING OF BONE

2.1 Introduction to bone microstructure

Bone in the skeleton is divided into two major macroscopically distinguishable categories: 1) cortical or compact bone, the shell or outer layer of bone which forms the shaft of skeletal elements such as the femur or humerus, and 2) trabecular or spongy bone, which forms a honeycomb-like mesh of rod and plate shaped trabeculae. The standard method of quantitatively describing the bone microarchitecture is the use of morphometric indices and parameters (Dempster et al. 2013). Using micro computed tomography (μCT), these measurements can be made in three dimensions non-destructively (Borah et al. 2001; Cooper et al. 2003). There is a large body of research developing on *in vivo* longitudinal scans, focused mainly on trabecular bone in small animals (Waarsing et al. 2004a) and humans (Boutroy et al. 2005), but with increasing interest in cortical bone. An *in vivo* study of the complete picture of cortical bone porosity so far remains out of reach.

2.1.1 Trabecular bone

The orientation of the trabecular network has long been known to align with major stresses; changes in the morphology of trabeculae have been linked to changes in disease state and have direct biomechanical consequences (Parfitt 1984). As a result, measuring and tracking these changes has direct relevance to questions in functional adaptation and health.

Trabecular bone quantification involves the direct measurement of parameters such as bone volume (BV), the full volume of the region segmented as bone, total volume (TV), and bone surface (BS), the surface of the region segmented as bone (Hildebrand et al. 1999), from which indices such as bone volume fraction (BV/TV), bone surface density (BS/TV), and

specific bone surface (BS/BV) can be calculated directly from two dimensional images, whether they are histological sections or μCT slices, or three dimensionally by counting voxels or using a volumetric marching cubes approach (Muller and Ruegsegger 1995).

From 3D μCT data parameters such as mean trabecular thickness (Tb.Th), mean trabecular separation (Tb.Sp) and mean trabecular number (Tb.N) can be directly calculated using sphere-fitting methods, which determine the thickness or separation based on the diameter of the largest sphere which is contained entirely in the trabeculae or spaces between them (Hildebrand and Ruegsegger 1997a). The mean trabecular number is the average number of trabeculae across a given unit length. It is calculated by taking the reciprocal of the addition of Tb.Sp and Tb.Th. One of the key advantages of direct 3D calculation of Tb.Th, Tb.Sp, and Tb.N, is that both mean values and the distributions of their variation can be obtained (Bouxsein et al. 2010). Several techniques to quantify the orientation of trabeculae exist, through the measurement of the degree of anisotropy. When the orientation of trabeculae are preferentially biased in one direction over another, then we say that they are anisotropic, while if they are evenly distributed in direction, they are isotropic. The degree of anisotropy can be quantified based off calculations of mean intercept length, volume orientation, star volume distribution, or star length distribution (Odgaard 1997). The mean intercept length (MIL) is the most commonly applied method, and is explored in depth in Figure 1. Connectivity is an important measure of networks, and is traditionally defined as the minimum number of connections that can be broken before the structure is divided (Odgaard and Gundersen 1993). In trabecular studies, measures of connectivity are based on the Euler number of the sample, a topological property (Kabel et al. 1999). Connectivity is typically measured as a connectivity density (Conn.D), the connectivity divided by the total volume of the region of interest. An index called the Structure Model Index

(SMI) is used to determine how the morphology of the trabeculae vary in general between idealized "rod-like" and "plate-like" types (Hildebrand and Ruegsegger 1997b). Trabecular bone has also been reported to be fractal in nature (Chappard et al. 2001) and as such a fractal dimension parameter can be calculated, representing an indication of the surface complexity of the bone and the complexity of branching trabeculae.

Abbreviation	Parameter	Description	Units
TV	Total volume	Total volume of a selected region of interest (ROI)	mm^3
BV	Bone volume	Volume of the ROI segmented as bone	mm^3
BS	Bone surface	Surface of the ROI segmented as bone	mm^2
BV/TV	Bone volume fraction	Percentage of the ROI which is segmented as bone	%
BS/TV	Bone surface density	Ratio of the bone surface area to the total volume	$mm^{2/} mm^3$
BS/BV	Specific bone surface	Ration of the bone surface area to the bone volume	$mm^{2/} mm^3$
Tb.Th	Trabecular thickness	Mean thickness of trabeculae	mm
Tb.Sp	Trabecular separation	Mean distance between trabeculae	mm
Tb.N	Trabecular number	Mean number of trabeculae per unit length	mm^{-1}
DA	Degree of anisotropy	Measurement of trabecular structural anisotropy	
Conn.D	Connectivity density	Measurement of the degree of trabecular connectivity over the volume	mm^{-3}
SMI	Structure model index	Measurement of the trabecular morphological structure	
D	Fractal dimension	Measurement of the trabecular surface complexity	

Table 2.1: Definition and description of 3D trabecular bone quantification parameters.

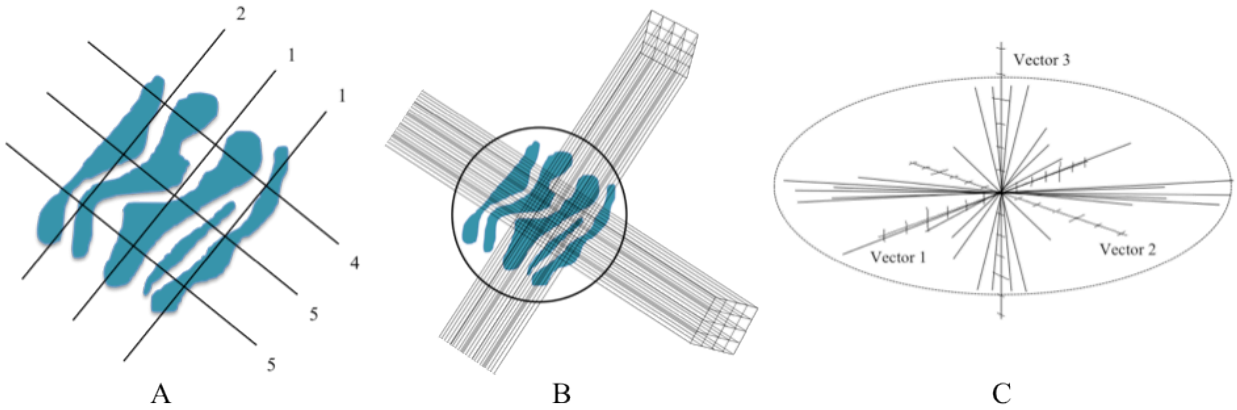

Figure 2.1: Illustration of the MIL method of DA calculation. The mean intercept length is found by passing a line through a 3D volume containing the region of interest, counting the number of intersections this line makes with part of the tissue (in this case bone) in the region of interest, and dividing this number by the length of the line. Differences in the MIL across different angles reflect the anisotropy in the bone. As seen in 'A', lines passing through the sample intercept the bone a different number of times depending on their orientation with respect to the anisotropy of the tissue. In 3D, many such lines are passed through the tissue ('B') to obtain MILs for a large number of angles to fully quantify the anisotropy over the whole volume. Next each line is drawn passing through the origin ('C'), and the resulting polar plot is fitted to a 3D ellipsoid with three main axes. The ellipsoid can be described as a tensor (3D matrix) with eigenvectors describing the strength of the anisotropy in the three major directions. From this tensor the DA can be calculated, by subtracting the division the maximum eigenvalue by the minimum eigenvalue from 1. The DA can then range from 0 to 1, where 0 is total isotropy and 1 is total anisotropy. Figure adapted from the CT-analyser manual (Bruker 2012).

2.1.2 Cortical bone

Cortical or compact bone forms the outer shell of material, surrounding the marrow cavity in long bones. In most mammals, primary cortical bone grows in the lamellar pattern, where layers of bone are laid down circumferentially around the endosteal and periosteal borders, and around blood vessels and nerve fibers, which form canals running through the bone. After the bone is initially laid down, a process known as remodeling occurs, where osteoblasts and osteoclasts work together in Basic Multicellular Units (BMUs) to carve new, secondary, canals through the existing bone tissue. As a result of this process, the cortical bone is perforated by a network of connected neurovascular canals. Changes in the geometry and morphology of these canals through remodeling have been linked to aging processes (Cooper et al. 2007b) and health status changes including the development of increased bone fragility and osteoporosis (Seeman 2002).

Quantification of cortical bone morphology generally is done at two different levels, the gross geometry of the bone and the morphology of the canal network. Gross measurements include total cross-sectional area (Tt.Ar), marrow area (Ma.Ar), cortical bone area (Ct.Ar), the periosteal (Ps.Pm) and endosteal (Ec.Pm) perimeters, and cortical thickness (Ct.Th). Characterization of the geometry is often done by application of beam theory, calculating cross-sectional second moments of inertia (I_{max}, I_{min}, I_x, I_y), and the polar second moment (J) for the bone. These moments can be related to bending strength and other mechanical properties of bone (Lieberman et al. 2004). Quantification of the canal network in three dimensions requires the use of μCT at a high resolution, typically with voxels of 10 microns or smaller (Basillais et al. 2007; Cooper et al. 2003), while quantification of the gross geometric parameters is possible at lower resolution, and can be done *in vivo* with current trabecular μCT protocols. Parameters including

tissue volume (TV), canal volume (Ca.V), canal surface (Ca.S) can be directly measured in three dimensions. Cortical porosity (Ca.V/TV) represents the relative volume of the canals within the tissue, the inverse of the trabecular bone volume fraction. Canal diameter (Ca.Dm) and canal separation (Ca.Sp) can be calculated based off the methods used for their trabecular analogues. Canal connectivity (Ca.ConnD) and canal length (Ca.Le) can be measured by using a skeletonization approach (Cooper et al. 2003) which measures the number of canal intersections, or nodes, and the distance between them. By measuring the angle of each skeletonized canal segment from the horizontal axis of the bone, canal orientation (Ca.Or) can be obtained (Britz et al. 2012b). The application of the structure model index (SMI) is relatively straightforward, as the idealized shape of a canal is similar to the ideal "rod-like" type in the SMI calculation. Basic Multicellular Units (BMUs) and associated resorption spaces within cortical bone can also be quantified with μCT using parameters including resorption space density and BMU range (Cooper et al. 2006).

Abbreviation	Parameter	Description	Units
Tt.Ar	Total cross sectional area	Total cross sectional area of the ROI	mm^2
Ct.Ar	Cortical area	Area of the ROI segmented as bone	mm^2
Ma.Ar	Marrow area	Area of the marrow cavity	mm^2
Ct.Ar/Ma.Ar	Cortical area fraction	Percentage of the ROI which is segmented as bone	%
Ps.Pm	Periosteal perimeter	Periosteal perimeter	mm
Ec.Pm	Endosteal perimeter	Endosteal perimeter	mm
Ct.Th	Cortical thickness	Mean thickness of the cortex	mm
I	Area moment of inertia	Measurement of resistance to bending, which varies in different directions, often indicated in subscript (I_x, I_y, I_{ap}, I_{ml}, I_{max}, I_{min})	mm^4
J	Polar moment of inertia	Measurement of resistance to torsion	mm^4
TV	Tissue volume	Volume segmented as bone	mm^3
Ca.V	Canal volume	Volume of the pores inside the bone	mm^3
Ca.S	Canal surface	Surface area of the pores inside the bone	mm^2
Ca.V/TV	Cortical porosity	Percentage of the tissue volume that is canal	%
Ca.D	Canal diameter	Mean canal diameter	mm
Ca.Sp	Canal separation	Mean distance between canals	mm
Ca.Conn.D	Canal connectivity density	Measurement of the canal connectivity over the tissue volume	mm^{-3}
Ca.Le	Canal length	Mean canal length	mm
Ca.Or	Canal orientation	Orientation of the canal away from the horizontal axis of the bone	°
SMI	Structure model index	Measurement of the canal shape	
	Resorption space density	Density of resorption spaces in cortical bone	spaces/mm^3
	BMU range	Mean length of BMUs	mm

Table 2.2: Definition and description of 3D cortical bone gross geometrical and microstructural quantification parameters.

2.2. Micro computed tomography

Micro computed tomography (μCT) was first used to image bone microstructure in 1989 (Feldkamp et al. 1989). Two main μCT systems exist which can be applied to the study of bone tissues, synchrotron x-ray sources and polychromatic microfocus x-ray tubes in so called 'desktop' systems which are often built and supplied by commercial vendors.

2.2.1 Synchrotron μCT

Synchrotron μCT is performed using x-rays produced as bremsstrahlung, or breaking radiation, created by the passage of an electron beam traveling near the speed of light through incredibly strong electromagnets. This x-ray beam travels down a beamline and is collimated, and can then be filtered by a monochromator if desired, selecting out x-rays in a narrow energy bandwidth of less than a hundred eV (Kinney et al. 1998). The number of x-ray photons passing through a given area over a given time, or flux, produced by synchrotron sources is several orders of magnitude greater than that produced by desktop sources (Kinney et al. 1998), which allows for this monochromation while still producing enough flux for imaging. A technical limitation of polychromatic imaging is the spread of x-rays with different energies which are differentially absorbed by tissue. As a result, the lower energy x-rays in the beam are absorbed faster in the tissue, while the higher energy end of the beam penetrates more easily. As a result, tissue areas of increasing thickness result in an increase in the average energy of the beam exiting the sample. In CT, this results in so called "beam hardening" artifacts, where the linear attenuation coefficients are artificially low in the interior of the sample and vice versa. Monochromatic beams allow for the measurement of the bone mineral density based on the differential absorption of x-rays by the bone tissue and, as the beam is very close to a single energy, avoids beam hardening artifacts in the reconstruction (Peyrin et al. 1998). Synchrotron

sources offer higher resolutions than typical desktop x-ray sources, with submicron level imaging, or nanoCT, becoming more common at these institutions (Andrews et al. 2010; Peyrin 2009; Schneider et al. 2007; Voide et al. 2009). Imaging at synchrotron sources can also take advantage of additional contrast mechanisms based on interactions between x-rays and matter other than absorption. Refractive index based imaging techniques including phase contrast (discussed further in Chapter 3) can provide improved visualization of smaller or more obscure targets. The disadvantages of synchrotron μCT are the limited access time, increased cost, and higher difficulty of use compared to common commercial systems.

2.2.2 Desktop μCT

Many commercial desktop μCT systems exist, using polychromatic microfocus x-ray tubes to image at high resolutions. These systems produce a cone shaped beam, which allows for geometric magnification but also increases blurring. The resolution of these systems is typically limited by the spot size of the x-ray tube, and their ability to image is limited by the current and energy of the tube. These two characteristics are intrinsically linked, as a smaller spot size limits the amount of current which can be applied across it without damaging the tube.

2.2.3 Dose

Radiation is the propagation of energy through a material. X-rays are a form of electromagnetic waves with moderately high quanta energy. These quanta or wave packets are called photons, and each carries a discrete amount of energy. As a beam of x-rays pass through material, the photons in the beam interact with the surrounding object, and may collide with its atoms. The atoms in the material absorb the energy from the photons, and this process ionizes electrons from the atoms. This ionization can disrupt molecular bonds and is therefore harmful to living tissues. The probability of an absorption happening is related to the atomic number (Z) of

a potential absorbing atom, and inversely proportional to the energy of the incident photon. What this means is that higher Z elements in tissue tend to absorb more x-rays than lower Z elements, and higher energy photons are absorbed less. Radiation dose is simply a measure of how much energy is deposited by the x-ray beam into the material, or in this case tissue. As the x-rays pass through the material, the beam is attenuated, and as a consequence the radiation exposure at the x-ray entrance point is higher than at the exit. In computed tomography this means that there is an uneven distribution of radiation in the object, with the center receiving the least amount of dose, and the surface being the highest. In small objects or samples, this effect is overshadowed by the difference absorption characteristics of different materials. For example, the bone in a limb will absorb more than the marrow it contains.

The ***absorbed dose*** is the energy deposited per unit mass of tissue, and is measured as joules per kilogram or grays (Gy). Closely related to the absorbed dose is the kerma, a term describing the kinetic energy transferred to charged ionizing particles from the x-ray beam per unit mass of the material. The key difference between absorbed dose and kerma is that the energy in the kerma is not necessarily contained in the location of the interaction between the beam and the tissue but may end up absorbed in a different place in the tissue. With regards to diagnostic x-rays, the absorbed dose and the kerma can be treated as equivalent(Bushberg 2002). Different materials will absorb different amounts of radiation, and therefore will have material specific kerma, and we may talk of air kerma, for absorption in air, or tissue kerma for absorption in soft tissue. Different sources of radiation can deposit differently into biological tissues, so a radiation weighting or quality factor, defined by the International Commission on Radiological Protection (ICRP), is used to convert the absorbed dose into a so called ***equivalent dose***, measured with units of sieverts (Sv). The weighting factor for x-rays is 1, so in this case

the equivalent dose and the absorbed dose will have the same value. A further quantity called the ***effective dose*** can be calculated for the radiation effects on isolated parts of the body, and is commonly in use for dosimetry in human studies using computed tomography and other radiometric methods. For reference, the tissue weighting factor for some selected tissue types are 0.01 for bone surfaces, 0.12 for red bone marrow, 0.01 for skin, 0.12 for the lungs, 0.12 for the colon, 0.08 for the gonads, and 0.04 for the thyroid (United Nations. Scientific Committee on the Effects of Atomic Radiation. 2010). The mean effective dose for some selected human CT examinations in first world heath care systems are 2.4 mSv for head, 7.8 mSv for thorax, 12.4 mSv for abdomen, 5.0 mSv for spine, and 9.4 mSv for the pelvis (United Nations. Scientific Committee on the Effects of Atomic Radiation. 2010). The dose for a single HRpqCT scan of the forearm is under 3 μSv (Boyd 2008). As a comparison, radiation from cosmic rays during airline flights create a mean effective dose of 38.7 μSv for a 7.7 hour flight from Chicago, IL to London, GB (Freidberg et al. 1999).

The computed tomography dose index (CTDI) is a radiation exposure index reported by a commercial CT manufacturer based on the average dose imparted to a phantom with a given acquisition protocol. It can then be used in conjunction with the body mass of the subject to calculate an absorbed dose. The CTDI values calculated do not always accurately reflect the patient dose, (McCollough et al. 2011) especially given the differences between modern and older commercial systems(Boone 2007).

2.2.4 Dosimetry

The two most common methods for measuring radiation dose in μCT imaging are ion chambers and thermoluminescent dosimeters (TLDs). Small ion chamber probes can be placed in the beam path to measure the air kerma during a scan, which can then be converted to the

absorbed dose (Shope et al. 1981). An ion chamber is a gas enclosed chamber with two electrodes, an anode and a cathode. A voltage potential applied across the electrodes creates an electric field in the gas. As x-rays pass through the chamber, they ionize particles in the gas, creating ion pairs of resulting positive ions and dissociated electrons. The electromagnetic field created in the chamber draws these particles to the anode and the cathode, creating an electric current which is proportional to the flux of the beam passing through. From this the dose can be calculated with reference to the ion chamber parameters. Ion chamber dosimetry is well established in the field, and is commonly used in μCT studies (Bayat et al. 2005; Brouwers et al. 2007; Klinck et al. 2008). Ion chambers need to be specifically calibrated for the energy range of the x-ray source. The other common method is the use of thermoluminescent dosimeters. TLDs are small inorganic scintillator crystals, in which electrons are trapped in excited states. If the crystal is later heated, the electrons return to their ground state and emit light. Measuring the emission of this light is proportional to the absorbed dose. The most common material used is lithium fluoride (LiF), because it exhibits very little release of the trapped electrons at room temperature. Also, the effective atomic number of the LiF crystal is close to that of soft tissue, meaning the absorbed dose in the dosimeter is closely proportional to a tissue dose over the energy range of imaging x-rays (Bushberg 2002). TLDs are useful as they are very small, and can be placed at specific locations on an animal, to measure dose in that specific target area. TLD dosimeters can also be implanted into animals to measure the deep tissue dose more directly and accurately (Figueroa et al. 2008). TLDs can either be sent offsite for measurement or used with thermoluminescent reader detectors and reused after an annealing cycle. Both ion chambers and TLDs are sensitive enough for use as dosimetry methods in small animal μCT (Bos 2001; Yu and Luxton 1999). OSL dosimetry is similar to TLD dosimetry, except the

crystals in use are read by subjecting them to selected frequencies of light instead of heat (Yukihara and McKeever 2008). A common crystal type is aluminum oxide, Al_2O_3:C (Yukihara et al. 2008).

2.2.5 Scan parameters impacting dose

The development of current μCT systems has been driven by a need for higher resolution and higher signal to noise (SNR) to accurately characterize microscopic features in bone and other hard and soft tissues. As the requirements for particular studies tend to vary immensely, μCT systems have been built with an ever increasing list of customizable scanning parameters, including the resolution/voxel size, rotation step, exposure time, and frame averaging. They also offer the ability to change the x-ray spectrum generated by changing the voltage across the tube in a desktop scanner or directly manipulating the energy of the beam emitted by a monochromator at a synchrotron, in combination with the use of thin metal foils for filtration of low energy x-rays(Boone et al. 2004). Changes in any or all of these parameters will affect the radiation dose absorbed in the animal, and they can be placed into three main categories: factors affecting the length of the radiation exposure, factors affecting the energy spectrum of the x-ray beam, and factors affecting the number of x-ray photons passing through a unit mass of material.

The tradeoff between image contrast and dose is clear. Image quality is improved by increased statistical collection of data, which increases the time spent by an animal in the beam, whether it is the number of rotations, the number of frames averaged, or the exposure time per frame. The ability to overcome noise is dependent on passing a sufficient number of photons through the tissue to provide contrast, which is equal to a requirement for spending enough time in the beam. Generally, for an increase of the signal or contrast to noise ratio by a factor of two will require an increase of the absorbed dose by a factor of four. At higher resolutions, passing

enough x-rays through smaller focal points in the material requires passing more x-rays through the whole material, and an improvement in resolution of a factor of 10 will increase the dose by a factor of 10^4 if the image quality is kept equivalent(Ford et al. 2003). Somewhat unintuitively, imaging with a higher kVp results in substantially lower doses. This is a result of lower absorption of higher energy x-rays in tissue. See figure 2 for details.

A Monte Carlo simulation by Boone et al(2004) showed that the use of higher energies lowered the mean dose significantly. The authors calculated that at 80 keV, a 20mm diameter animal would absorb a mean absorbed dose of 34.075 μGy per 10^6 photons/mm^2 at the isocenter of the beam, while at 25 keV the dose was 89.563 μGy, more than 2.5x higher. Significant increases in dose were found for higher kVp as well. A reduction in dose can be achieved by shaping the x-ray spectrum to increase the mean energy of the beam. Using 0.5-2mm metal filters cuts out low energy emission peaks from elements used in the x-ray tube such as tungsten (Boone et al. 2004) and shifted the peak in the x-ray spectrum to a higher energy. This has two drawbacks, it lowers the flux of the system leading to a necessity for longer exposure time to achieve the same statistics, and imaging at higher energy results in lower image contrast. Since the reduction in dose is due to less absorption in the tissue, a concurrent effect is the reduction in attenuation contrast in the resulting images. A trade-off must be found here, between the lowering of contrast at high energy and the resulting need for an increase in exposure time.

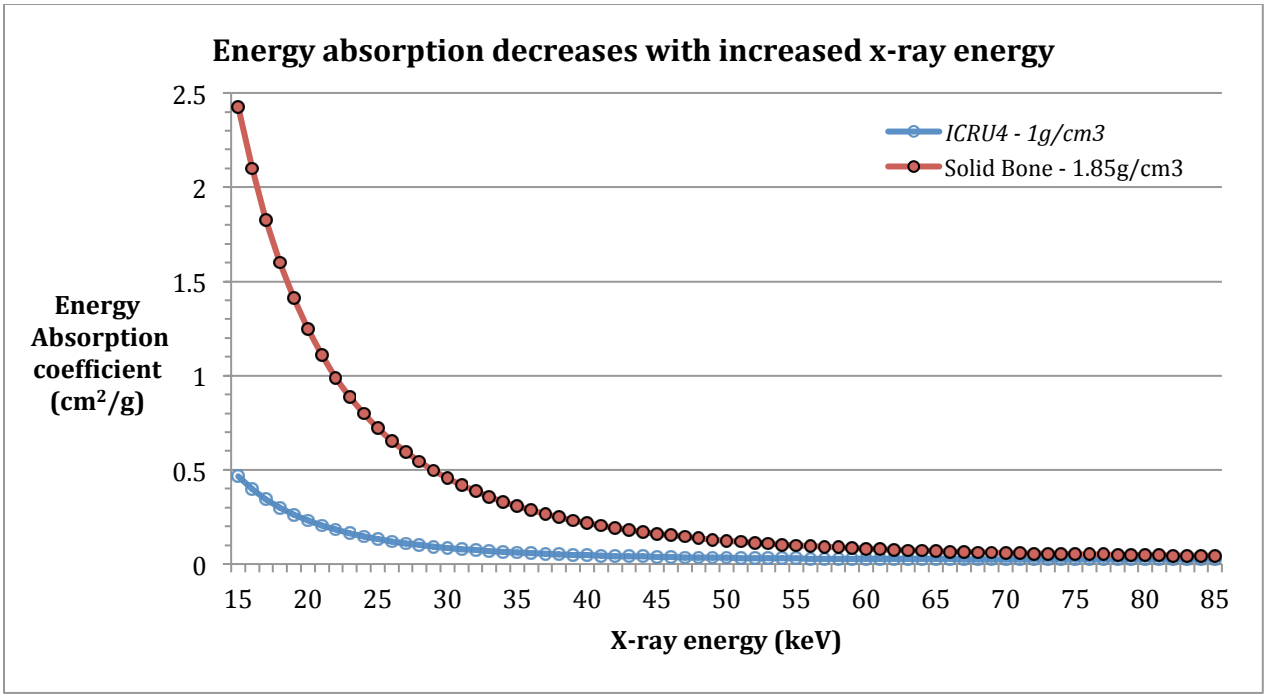

Figure 2.2: The energy absorption coefficients for soft tissue (ICRU4 NIST standard) and solid bone (NIST) in cm^2/g plotted against energy, showing the decrease in energy absorption, and therefore absorbed dose, with higher x-ray energy. (Data from NIST, http://www.nist.gov/)

2.3 Small animal µCT *in vivo*

The ability to image trabecular bone in small animals requires a much higher resolution than imaging in humans, simply due to the size difference between the corresponding trabecular structures. A meta analysis of trabecular parameters found that Tb.Th in humans ranges from about 83-296 µm, in rats from 50-115 µm, and in mice from 22-69 µm (Barak et al. 2013). As a result, the options for small animal (typically rat or mouse) imaging are limited to x-ray based µCT imaging, while options for human trabecular analysis include micro magnetic resonance imaging (µMRI) with 137 µm voxels and high resolution peripheral quantitative CT (HRpqCT) with 82 µm voxels (Krug et al. 2008). These imaging systems are not able to fully measure trabecular parameters in 3D and so-called semi-derived algorithms are used (Buie et al. 2007). Beginning in the early 1990's high resolution *in vivo* µCT imaging of small animal trabecular bone was pioneered using monochromatic synchrotron x-ray sources (Kinney et al. 1995; Lane et

al. 1998). These efforts ultimately lead to the development of commercial desktop *in vivo* μCT scanners using polychromatic micro-focus x-ray tubes (David et al. 2003; Waarsing et al. 2004a). *In vivo* scanning of laboratory animals allows for the design and application of longitudinal studies, which have more power to detect causal relationships and make the direct observation of development possible in a single animal. Using a single study population provides data that is internally consistent and reduces the number of animals needed for the study. Dynamic data across the lifespan of a single individual are able to track shifts in individual trabeculae using 3D registration techniques (Waarsing et al. 2004b). This allows for localization and quantification of bone formation and resorption across the trabecular network (Boyd et al. 2006b; Schulte et al. 2011). As such, they increase the options available to researchers for experimental studies of bone. The main limitation of *in vivo* μCT scanning is the radiation dose imparted to the animal. In addition to this, any movement by the animal will cause artifacts in the reconstructed image, so the area of interest must be securely held in place. Animals must be imaged under anaesthetic, to prevent such movement, either through the use of injectables, such as pentobarbital sodium or a combination of ketamine and xylazine, or more commonly using gas anaesthetic, typically isoflurane. The amount of time an animal can be kept under anaesthetic is limited with injectable anaesthetic as it is increasingly difficult to titrate an appropriate dose because the injectable drugs are metabolized at different rates in each individual animal. Gas anaesthetic allows for the plane of anaesthetic to be specifically tailored to each individual animal throughout the scan.

The absorbed dose is to an approximation inversely proportional to the fourth power of resolution, so that any increase in resolution will have a corresponding strong increase in dose. It is for this reason that *in vivo* studies of cortical porosity, requiring approximately double the resolution as studies of trabecular bone, have remained out of reach. In humans and rats, average

Ca.D of 173±45 μm and 36±12 μm respectively were reported by Jowsey (1966) based on histological examination of the femur. Cooper et al (2007a) reported a mean Ca.D of 68.0 μm in humans and noted that cortical parameters had a significant dependence on resolution, with analysis becoming less stable with voxels greater than 10μm. Matsumoto et al (2006) found mean Ca.D of 17.5 μm in the tibiae of rats and noted that the smallest canals were 1 voxel (5.83μm) across, indicating that higher resolutions might be necessary to capture the full cortical pore network.

2.3.1 Synchrotron in vivo μCT

Kinney et al (1995) were the first to perform *in vivo* μCT using a synchrotron, at the Stanford Synchrotron Radiation Laboratory (SSRL) in the United States on the x-ray wiggler beamline 10-2. They used 25 keV x-rays from a single crystal silicon monochromator with a charge-coupled device (CCD) detector. This instrument is known as the X-ray tomographic microscope (XTM) (Kinney et al. 1992). Kinney et al. (1995) were able to keep imaging time at less than 30 minutes per rat and used shuttering to reduce the beam exposure to the animal. A lead shield was used to cover the body of the rats during the scan, reducing the body's exposure to scattered radiation. Anaesthetized Sprague-Dawley rats received a quoted dose of no more than 90 rads (0.9 Gy) to a 2mm high target area in the proximal tibia. Half the group was ovariectomized after the scan and all were scanned again 5 weeks after the first imaging session with the same parameters. Measurements of BV/TV, Tb.Th, Tb.Sp, and Tb.N were made. The voxel size and rotation step used for imaging were not specified, and the method for the dose calculation was not described. Further studies were performed at SSRL by the same group (Lane et al. 1999; Lane et al. 2003; Lane et al. 1998) with 23 μm voxels; however, the radiation doses and rotation steps were not specified in these studies. Another experiment quotes a rotation step

of 1°, leading to 180 projections (Kinney et al. 1998), but does not specify the resolution used or the radiation dose. Despite the great potential put forward by these studies at SSRL, studies of dynamic changes in trabecular bone architecture using *in vivo* synchrotron μCT remained few and were slow to appear, likely due to the limited nature of beamtime and the inherently difficult nature of synchrotron imaging. Bayat et al. (2005) published a study on the C3H/HeJ and C57BL/6J strains of mice, imaging at the ID19 beamline at the European Synchrotron Radiation Facility (ESRF) in France. Using the wiggler beam they imaged with a so-called monochromatic energy between 20-24 keV, and a 0.5 mm aluminum filter. A pixel size of 10 μm was used along with rotation steps between 0.3° and 0.5°. Under these conditions they found a dose in the range of 2-20 Gy, depending on parameter choices (Bayat et al. 2005). They report higher image quality as the dose increases, and chose comparison points of 2.3, 7.5, and 14.5 Gy with no significant differences in mineralization between the 7.5 and 14.5 Gy dose levels. They also note no apparent damage to the mice. Coan et al (2010b) published a study using *in vivo* analyzer-based imaging (ABI), hereafter referred to as diffraction enhanced imaging (DEI), of guinea pigs. Using the ID17 biomedical beamline at the ESRF, imaging at 52 keV with 47 μm pixels. DEI uses an additional, analyzer, crystal to enhance the image contrast through refraction of the x-ray beam at material or geometrical interfaces in the sample. They quote a skin entrance dose of 0.15 mGy per projection image. DEI-CT at a 0.24° rotation step through 360° would then produce approximately 225 mGy per scan. Matsumoto et al. (2011) published a short term study on bone dynamics in an unnamed strain of mice at the Experimental Animal Facility and Biomedical Imaging Center of the Super Photon ring-8 GeV (SPring-8) synchrotron in Japan. They used the bending magnet beamline 20B2, imaging in Hutch 3, imaging at 25 keV. Imaging was performed with 11.7 μm pixels and 0.2° rotation steps, leading to a quoted dose of 5.0 Gy

(Matsumoto et al. 2011). They note this level of radiation dose is high enough to inhibit cell proliferation and induce cell death in osteoblast cultures (Dare et al. 1997; Matsumura et al. 1996) and reduce the ability of the bone to grow in the long term. Synchrotron radiation was also used by Choi et al. (2010) to perform *in vivo* projection based in-line phase contrast imaging on DBA/1J mice with collagen induced arthritis (CIA). The animals were exposed using a polychromatic beam produced at the 1B2/microprobe beamline at the Pohang Light Source (PLS) in Korea. The energy range of the beam was 7-14 keV which produced doses between 0.8 and 3 Gy per image with a spatial resolution of 1.48 μm.

The advantages of synchrotron imaging are its high resolution and adaptability, high flux at a wide energy range, monochromaticity, and the potential for imaging using refractive index based contrast; however, synchrotron sources also tend to produce higher doses, beamtime is limited, set-up can be difficult and few synchrotrons have established *in vivo* imaging programs. In addition, the fixed nature of the source means that the animal must rotate in the beam, complicating the imaging process and requiring a more precise stage setup. A synchrotron source cannot match the ability for high throughput of a desktop x-ray tube source, though this throughput comes at the expense of lower contrast and resolution.

2.3.2 Desktop in vivo μCT

Because of the limitations of synchrotron imaging, many teams were quick to develop desktop x-ray sources capable of high resolution imaging, centered around the ability to image an animal *in vivo* (Kohlbrenner et al. 2001; Paulus et al. 1999; Ruegsegger et al. 1999; Sasov 2002; Sasov and Dewaele 2002). Although synchrotron sources are able to image at higher resolution, Peyrin et al. (1998) determined that 14 μm was sufficient to give a reasonably good quantification of the trabecular architecture, a resolution which is commonly achievable in

desktop systems. These systems are built around either stacked fan beam x-ray sources (Kohlbrenner et al. 2000) or cone beam tubes (Reimann et al. 1997). Much of this work was done either by or in collaboration with scientists from commercial enterprises, and in the early 2000's a number of studies used prototype commercial μCT scanners designed for *in vivo* imaging. David et al. (2003) used a prototype system built by ScanCo medical, a VivaCT 20. This system acts, as is typical with desktop *in vivo* systems, using a rotating gantry, where the x-ray source and detector rotate around the object being scanned. This allows for straightforward continuous flow of gas anaesthetic during a scan, as well as a consistent static geometry of the animal in the scanner, reducing the chance of movement of extraneous body parts during the scan. The VivaCT 20 has anisotropic voxels of 20 x 20 x 26 μm, similar to the resolution used in *in vivo* synchrotron scanning. No radiation dose is quoted. Similarly, Waarsing et al. (2004a) published a study using a prototype SkyScan 1076 μCT scanner. This system operates with a rotating gantry, and has a 100 kV tube with a spot size of 5 μm. Projections were taken with voxels of 10 μm, which was then undersampled to 20 μm voxels in the reconstruction. Scans lasted 20 minutes and produced roughly 0.4 Gy, measured by "a dosimeter". The tibia was scanned as it can be easily stretched back and isolated from the rest of the body, reducing radiation dose to the core of the animal.

Since the first pioneering studies, development in the μCT industry has proceeded rapidly, and scanning systems use rotating gantry cone beam micro-focus x-ray tubes and can achieve resolutions between 9-100 μm, performing scans in under 20 minutes. They provide filtration options for the beam, using thin metal foils of aluminum, copper, or other metals, and have a wide energy bandwidth (ranging from 20 to over 100 keV). The incredible amount of options available to the researcher, from the system level down to the parameter level, means

that predicting the dose imparted by a scan can be challenging, and achieving the requisite contrast at the required resolution may incur a dose that is not tolerable for the wellbeing of the animal.

2.3.3 Effects of radiation dose on bone

Given the number of parameters that can affect the radiation dose in a given protocol, it is important to establish what level of dose can be tolerated. Side effects from overdose can have a direct influence on the skeletal system, and the level of dose a scan creates can cause different effects. Discrepant results have been found concerning the doses required before changes to the bone microarchitecture can be detected in rodents, and these effects have not yet been fully investigated.

The primary mechanism for cell death in irradiated tissue is DNA single and double-strand breaks after ionization by the x-ray beam (Olive et al. 1990). This damage initiates DNA repair processes and can decrease cell proliferation (Iliakis et al. 2003). Studies *in vitro* have shown that radiation doses of 4 Gy and above inhibit osteoblast growth and proliferation (Dare et al. 1997; Dudziak et al. 2000; Gal et al. 2000), and while a 2.5 Gy dose has been shown to stimulate osteoclast activity (Scheven et al. 1985), a 2 Gy dose was shown to inhibit osteoclast activity (Willey et al. 2008). It is well accepted that proliferating cells are more sensitive to dose, and radiation damage to cells such as growth plate chondrocytes and red marrow bone cells may cause more obvious defects (Bisgard and Hunt 1936; Huang et al. 2009). Imaging away from the growth plate may therefore reduce the physiological impact of the radiation dose created in a scanned animal. While bone cells are sensitive to radiation, it is important to understand the response of the cells in the context of their tissue. In addition, it is important to differentiate the effects of a whole body dose from those resulting from irradiation of only a small part of a limb.

In humans a whole body dose of 250 mGy can lead to reduced lymphocyte counts (Bushberg 2002); however, physiological responses to whole body doses will differ from partial limb irradiation.

A single dose of 5 Gy to the tibial metaphysis has been shown to impair bone regeneration in rats, with no effects found using a 2.5 Gy dose (Jacobsson et al. 1985). In rats, a study with 8 weekly scans at 939 mGy showed no significant difference in bone architectural parameters, or in the viability of the bone marrow cells (Brouwers et al. 2007). A study of rats with 7 monthly scans at 0.5 Gy showed significant decreases in trabecular structural parameters (Boyd et al. 2006a). The authors suggest this may be due to normal aging but it is consistent with effects resulting from radiation. In this study the dose was not measured but calculated by software provided by the manufacturer and it may be possible that this calculated dose is underestimating the true radiation dose to the animals. A study in C3H/HeJ (C3H), C57BL/6J (BL6), and BALB/cByJ (BAL) mice strains and Wistar rats used 4 or 5 scans for the OVX mice, 4 for the control mice, and 6 scans for the rats. Doses of 712 mGy for the mice protocol and 503 mGy for the rats were measured used an ion chamber probe (Klinck et al. 2008). They found no significant differences in the bone architecture of the rats but found small significant differences in the trabecular architecture and cortical geometry of the mice, which while detectable did not obscure the overall trend of the effects of the ovariectomy treatment used in the higher bone mass strains (BAL and C3H) with a less clear distinction in lower bone mass strains such as the BL6. Another study on C57Bl/6 (BL6) mice scanned 3 times separated by 2 week intervals using doses of 776 mGy, 434 mGy and 166 mGy. Significant changes were found in the 776 mGy scans but for the 434 mGy and 166 mGy scans no significant effects were found scans on the trabecular or cortical architecture as well as no hematological side effects (Laperre et al. 2011);

however, decreasing the dose from 776 to 434 mGy resulted in lowered image quality as expected.

An emerging trend in the literature is that the ability to tolerate dose varies not just between rats and mice but also between the various breeds of these animals. While some synchrotron studies image at high resolution with high doses that can be an order of magnitude larger than those used in desktop μCT systems (Bayat et al. 2005; Matsumoto et al. 2011), controls for radiation effects must be made. Using the non-irradiated contralateral limb along with a control group is essential. Other potential confounding factors include the age of the animals in the protocols, as young growing animals experiencing more rapid cell division will be more sensitive to radiation effects, which can more easily retard growth (Mitchell and Logan 1998).

In order to image cortical bone porosity *in vivo*, doses on the same order as those used in trabecular *in vivo* imaging must be achieved, with an upper boundary set by those studies done at synchrotron sources. A dose of 5 Gy is the maximum used with the most common doses lying between 0.5 and 1.0 Gy. Achieving doses of this level while scanning at the higher resolution (at or below 10 μm pixels) required to capture the cortical network *in vivo* will be difficult. Advanced synchrotron imaging techniques which use contrast derived from refraction or interference may be required in order to longitudinally image cortical bone porosity in small animals without any radiation effects.

Publication	Resolution	Energy	Dose	Animal	Target	Number of Scans	Age of animals	Sex of animals
(Kinney et al. 1995)	N/A	25 keV	0.9 Gy	Sprague-Dawley rats	Proximal tibia	1	6 months	Female
(Kinney et al. 1998)	N/A	25 keV	N/A	Sprague-Dawley rats	Proximal tibia	3	6 months	N/A
[46]	23 µm	25 keV	N/A	Sprague-Dawley rats	Proximal tibia	5	6 months	Female
(Lane et al. 1999)	23 µm	25 keV	N/A	Sprague-Dawley rats	Proximal tibia	3	6 months	Female
(Lane et al. 2003)	23 µm	25 keV	N/A	Sprague-Dawley rats	Proximal tibia	3	6 months	Female
(Bayat et al. 2005)	10 µm	20-24 keV	2-20 Gy	C3H/HeJ, C57BL/6J mice	Knee	1	12 weeks	N/A
(Coan et al. 2010b)	47 µm	52 keV	225 Gy	Dunkin Hartley guinea pigs	Hip, knee	1	6 months	Male
(Matsumoto et al. 2011)	11.7 µm	25 keV	5.0 Gy	Mice	Proximal tibia	2	13 weeks	Male
(Choi et al. 2010)	1.48 µm	7-14 keV	0.8-3.0 Gy	DBA/1J mice	Forepaw	1	6 weeks	N/A

Table 2.3: Synchrotron protocols and their major features

Publication	Resolution	Energy	Dose	Animal	Target	Number of Scans	Age of animals	Sex of animals
(David et al. 2003)	26 µm	n/a	n/a	Wistar rats	Proximal tibia	4	4 month	Female
(Waarsing et al. 2004a)	10 µm	100 kV	0.4 Gy	Wistar rats	Proximal tibia	3	10 month	Female
(Brouwers et al. 2007)	15 µm	70 kV	0.939 Gy	Wistar rats	Proximal tibia	8	30 week	Female
(Boyd et al. 2006a)	15 µm	55 kV	0.5 Gy	Wistar rats	Proximal tibia	7	8 month	Female
(Klinck et al. 2008)	10 µm	55 kV	0.712 Gy for mice, 0.503 Gy for rats	C3H, BL6, BAL mice, Wistar rats	Proximal tibia	4 for control mice, 5 for OVX mice, 6 for rats	12 week old mice, 8 month old rats	Female
(Perilli et al. 2010)	8.7 µm	74 kV	N/A	Sprague–Dawley rats	Proximal tibia	5	2 month	Female
(Laperre et al. 2011)	9 µm, 18 µm	50 kV	0.776 Gy, 0.434 Gy, 0.166 Gy	BL6 mice	Proximal tibia	3	4 week, 10 week, 16 week	Male
(Lambers et al. 2012; Lambers et al. 2011)	10.5 µm	55 kV	0.640 Gy	BL6 mice	Caudal vertebrae	5	14 week	Female
(Campbell et al. 2011)	12.5 µm	55 kV	0.338 Gy	Wistar rats	Proximal tibia	9	7-9 months	Female

Table 2.4: Desktop µCT protocols and their major features

2.4 Conclusion

In vivo imaging opens new doors for researchers. Three dimensional registration of bone measurements allows for the detection and tracking of individual trabeculae in single animals (Boyd et al. 2006b; Nishiyama et al. 2010; Waarsing et al. 2004a). The potential for the use of these techniques is only beginning to be explored, and will have great impact in preclinical studies on pharmacological interventions and transgenic models. Longitudinal *in vivo* imaging depends on confidence in the measurements made. Given that radiation dose is known to affect the processes of bone development, it is important to fully quantify the effects of radiation to the bone and plan scan protocols to minimize its impact. The study of cortical bone architecture *in vivo* remains outside the grasp of conventional absorption methodology, as current imaging methods do not have the resolution required for complete quantification of the canal structure within cortical bone. The increase in resolution required for sufficient signal to noise puts the dose outside the safe and feasible imaging range; however, *in vivo* imaging of cortical porosity will be essential before the progression of remodeling can be fully elucidated. Advanced synchrotron methods dependent on refraction or phase contrast will be needed in order to overcome these limitations and bring the dose into a feasible regime.

CHAPTER 3: PHASE CONTRAST SYNCHROTRON μCT

3.1 Introduction

Cortical bone is a dynamic tissue that undergoes adaptive and pathological changes throughout life. A full understanding of the nature of these changes is important to understand both healthy and abnormal changes in cortical bone, an integral part of the entire skeleton. This understanding however remains far from complete. Existing studies have been cross-sectional and *ex vivo* (Britz et al. 2010; Cooper et al. 2003; Jast and Jasiuk 2013; Particelli et al. 2012; Schneider et al. 2007) and do not represent the full subtlety of the slow processes involved in bone renewal. The process of remodeling is an essential component in disease pathways in osteoporosis and the structures involved in remodeling, basic multicellular units (BMUs), represent a biological signal which reflects the functional environment of a bone throughout life and the health of an individual. The study of cortical microstructure still largely depends on studies based on 2D histological techniques, limiting the appreciation of the intricate 3D network. Furthering the understanding of the complex interplay between bone formation and resorption through the remodeling process will depend on the ability to image cortical porosity *in vivo*. The details of BMU progression, including their rate of travel and change in 3D orientation and morphology over time, likely require longitudinal studies to unravel. While rats do not normally undergo remodeling, their size and the amount of previous work done on different strains makes them the best choice for cortical bone study. Remodeling can be easily induced using a variety of methods, including fatigue loading and calcium restriction models (Bentolila et al. 1998; Carter 1984; Kubo et al. 1999; Lieben et al. 2010). The ability to quantify BMU morphology and cortical porosity *in vivo* using μCT will require a new approach as the high

resolution necessary brings a corresponding high radiation dose which has been found to disrupt trabecular bone growth and remodeling processes (Klinck et al. 2008; Laperre et al. 2011).

Phase contrast μCT has been shown to have potential for imaging cortical microarchitecture including porosity (Arhatari et al. 2011; Cooper et al. 2011b) and osteocyte lacunae (Carter et al. 2013; Langer et al. 2012) at even higher resolutions. Synchrotron Phase contrast has the potential to lower the radiation dose by enabling higher energy scanning than is typically possible in a desktop μCT system. The use of high energy synchrotron phase contrast at high resolution could bring the dose into the range used by conventional x-ray sources and allow longitudinal studies of cortical bone porosity.

3.2 Phase contrast

The first commercial computed tomography system was developed in 1973 (Hounsfield), for which G. N. Hounsfield and A.M. Cormack shared the 1979 Nobel Prize in Physiology or Medicine. Traditional CT relies on differential x-ray absorption across materials or tissue types. A series of projection x-ray images are taken of an object rotated at angles from 0 to 180 degrees, from which the 3D shape of the object can be reconstructed. Each pixel in the projection images represents a line integral of the x-ray energy absorption coefficients in the path through the object. The denser a material is to x-rays, the darker the resulting image will be. From the full series of projections, the integrals can be solved for the different absorption coefficients of the different materials in the object, creating a 2D map of the absorption coefficients that is parallel to the x-ray beam path through the object. In the reconstruction the image gray levels are inverted so that the background is dark and areas of higher absorption are bright. The energy from the x-rays absorbed in the tissue typically remains in the tissue, creating a radiation dose directly related to the contrast in the image.

Phase contrast imaging is characterized by excellent image quality, enhanced contrast and increased tissue discrimination. Conventional medical imaging systems use polychromatic beams and rely almost entirely on x-ray absorption, ignoring information produced by scattering within the tissue. This phase shift, produced as photons pass through the tissue and scatter, is capable of generating significantly enhanced contrast (Zhou and Brahme 2008). The resulting phase contrast decreases less rapidly with increasing x-ray energy than absorption contrast, and is more tolerant to noise. Several methods of exploiting the phase shift exist and have been incorporated into synchrotron techniques, and use a monochromatic beam produced by a perfect crystal. Most of these methods, including diffraction enhanced imaging, and interferometry or diffraction grating phase contrast, use further crystal optics to refine the x-ray beam (see figure 3.1).

Diffraction enhanced imaging (DEI) uses a so called analyzer crystal between the object and the detector (see figure 3.1). As the x-ray beam passes through the object, it refracts across tissue or material interfaces in the sample, changing the angle of different parts of the beam. The analyzer crystal acts similar to a diffraction grating, and allows only a very narrow range of those angles through. By changing the angle the analyzer crystal is positioned at, it is possible to take images recording different refraction angles and to extract the phase and absorption components of the image (Chapman et al. 1997; Zhu et al. 2011). DEI has been used as a low dose method to enhance imaging capabilities in mammography (Hasnah et al. 2002; Pisano et al. 2000) and to visualize cartilage, which is typically transparent to x-rays (Izadifar et al. 2013; Mollenhauer et al. 2002). DEI has also been used to investigate trabecular and cortical bone, as a novel method for microarchitecture visualization (Coan et al. 2010b; Cooper et al. 2011a).

Interferometry is thought to be the most sensitive phase detection method as the refraction from the tissue is detected as interference fringes which are inversely related to the

deflection angle (David et al. 2002). When this deflection angle is large, as happens in interfaces between tissue types with structural boundaries with large differences in refractive indices, the fringes may become too narrow to be resolved (Zhou and Brahme 2008). These issues may be resolved by using phase gratings instead, creating a so-called Talbot interferometer (Pfeiffer et al. 2008). By placing a series of phase gratings along the beam path, one between the x-ray source and the sample, and two between the sample and the detector, deflections created in the sample can be detected (see figure 3.1). The first grating, called the source grating G0, is placed close to the x-ray source and converts the beam into a coherent virtual line source. Using this grating means that conventional polychromatic x-ray sources can be used, and commercial systems using this method of phase contrast are under development for human (Donath et al. 2010) and small animal (Pauwels et al. 2012) imaging. The second grating, the phase grating G1, creates a phase modulation on the beam, and the third grating, the analyzer grating G2, is placed immediately in front of the detector and converts this into an intensity modulation, which appears as conventional x-ray contrast on the detector.

Propagation or in-line phase contrast is a refractive index based source of contrast that comes from interference of x-rays in the object (Snigirev et al. 1995). In a typical synchrotron parallel beam absorption based CT scan, the object is placed very close to the detector so as to minimize any geometrical distortion from the x-rays spreading out over time, whereas in a phase contrast set-up, the object is placed at a distance from the detector (see figure 3.1). In desktop μCT systems, this geometrical distortion is often exploited to produce magnification of voxels and increase the resolution of the system. In these cases the small distances involved and the polychromatic nature of the beam means that no significant phase contrast is typically in the

images, though optimization of the geometry of a system can produce phase effects (Sassov and Van Dyck 2000).

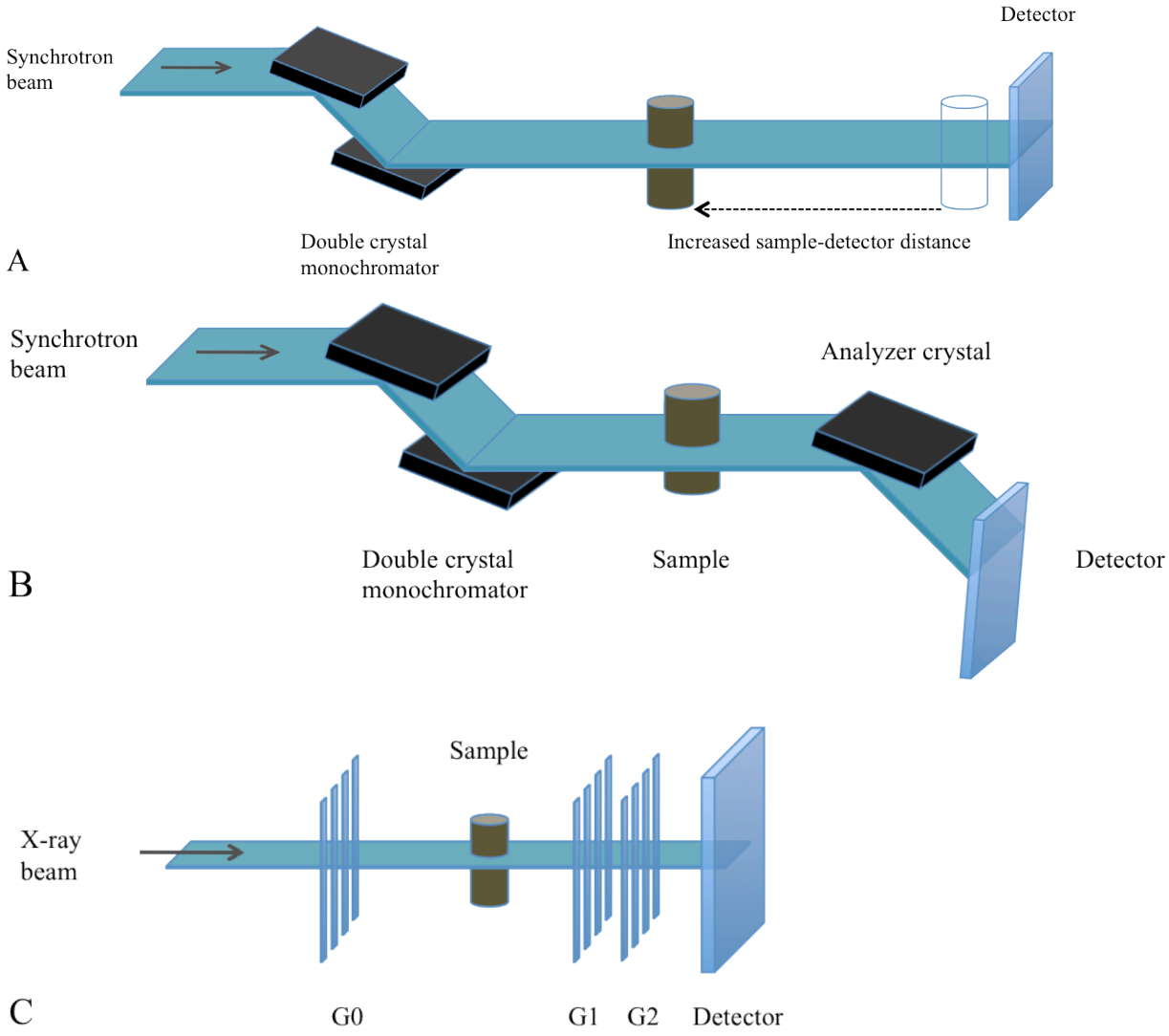

Figure 3.1: Phase contrast imaging setups. In A, the setup for propagation phase contrast is shown, with the increased sample-detector distance. In B, the setup for DEI is shown, with the analyzer crystal. In C, the setup for grating based phase contrast is shown, with the source grating G0, the phase grating G1, and the analyzer grating G2.

Variations in thickness and x-ray refractive index due to changes in the composition and density of materials in the object being scanned influence the phase of the x-rays that are detected. This leads to excellent contrast in soft tissue compared to absorption imaging, where the different soft tissue types are often unable to be differentiated from each other and water due to their similar absorption coefficients (Momose et al. 1996). Phase contrast is used to visualize tissues such as cartilage (Coan et al. 2010a), organ tissue including breast, brain and lung (Lewis 2004), and blood vessels without contrast agents (Momose et al. 2000). Phase contrast has also been used to examine fossilized hard tissues including bone and teeth (Betz et al. 2007; Lak et al. 2008; Smith et al. 2007; Smith et al. 2010; Tafforeau et al. 2006). X-rays passing through an 'edge' at the junction of two different materials are bent slightly, leading to changes in the x-ray wavefront that propagate over the distance between the object and the detector (see figure 3.2).

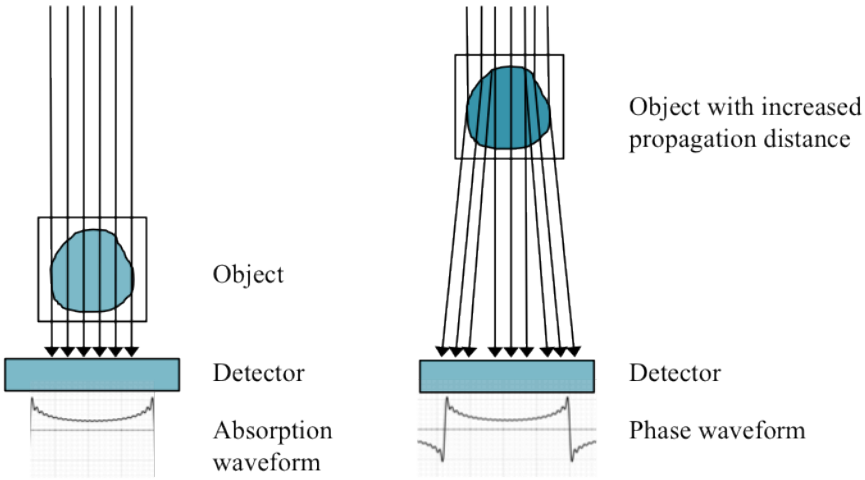

Figure 3.2: Changes in the x-ray waveform through the use of propagation phase contrast.

Because phase contrast depends on x-ray transmission through the target, its effectiveness at high x-ray energies is better than absorption contrast. This is a critical factor in the ability of

phase contrast protocols to lower radiation dose as imaging at higher energies reduces dose. The resulting effect is that the interfaces between materials of different x-ray absorption are highlighted by a fringe of bright and dark regions on the detector where the x-rays have been bent into distinct regions of high and low absorption on the detector. The width of these lines is dependent on the propagation distance between the object and the detector, and by varying this distance the width of these lines can be optimized to show a bright, easily distinguishable border, while preserving an accurate dimension of the highlighted structures. Imaging in cortical bone leads to a 'halo' around the periosteal and endosteal borders, as well as the edges of cortical canals and osteocyte lacunae (Britz et al. 2012a; Carter et al. 2013). Phase contrast at extremely high resolution is able to delineate osteons boundaries in cortical bone (Cooper et al. 2011b). The optimal phase distance to effectively delineate tissue boundaries depends on both the energy of the x-ray beam and the target resolution. Too large of a propagation distance will cause blur in the images as the phase shifts increase in magnitude, while too small of a distance restricts the divergence possible in the beam (Kotre and Birch 1999).

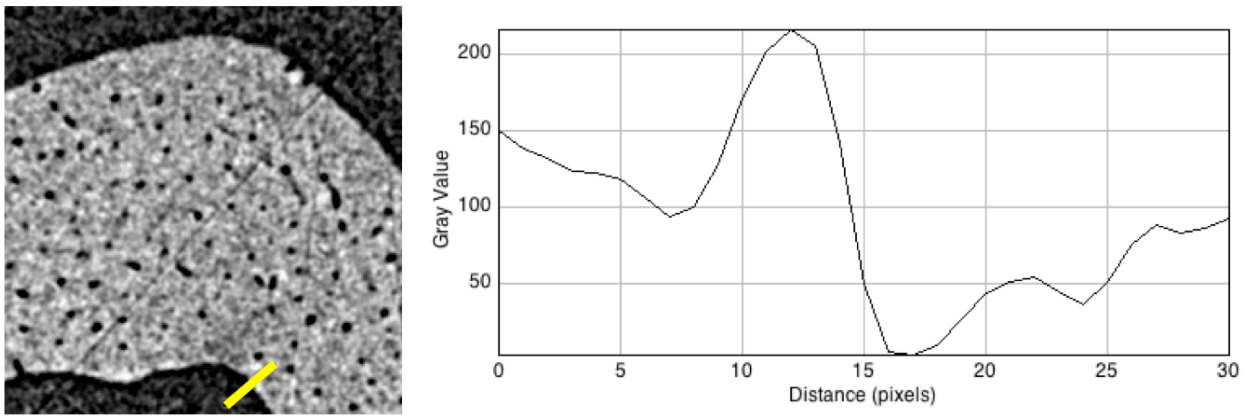

Figure 3.3: The edge-enhancement effect can be seen in the graph on the right, where the bone tissue is on the left and the background is on the right. The phase peak has gray levels higher than the bone and lower than the background. The area in the graph is shown as the yellow line in the synchrotron μCT slice on the left.

While phase contrast imaging can be done using a polychromatic source (Wilkins et al. 1996) and commercial phase contrast systems are under development (Pauwels et al. 2012), these systems are not able to image at resolutions high enough for imaging cortical porosity or use gratings which, while producing excellent soft tissue contrast, are unsuitable for bone imaging as the bone produces too much of a phase shift and causes streaking artifacts (Tapfer et al. 2013). In-line phase contrast also has the advantage of requiring little additional set-up compared to absorption contrast, whereas grating based phase contrast requires the use of an interferometer in the beam. Other phase contrast techniques including diffraction enhanced imaging (DEI) may have potential for *in vivo* imaging (Coan et al. 2010b) but also require additional crystal devices and are subject to their other drawbacks as well. Human cortical porosity was able to be imaged *ex vivo* using DEI in humans at lower resolution than is possible through absorption contrast (Cooper et al. 2011a), but has not been explored in laboratory animals or in CT *in vivo*.

As mentioned in Chapter 2, the impact of parameters such as the energy spectrum of the x-ray beam, the amount and type of filtration used, the number of projection images acquired, the resolution, and the exposure time all have a great impact on the dose created in the animal being scanned, so I set out to optimize the phase contrast protocol to produce sufficient image quality to visualize cortical porosity while maintaining a feasible radiation dose. By controlling the number of projections, frame averaging, exposure time, and x-ray beam energy with around 10 μm voxels, my goal was to lower the radiation dose to a feasible level for longitudinal imaging. By manipulating the phase propagation distance, I aimed to visualize cortical porosity at this resolution, and perform μCT to make these measurements at this resolution *in vivo*.

3.3 Materials and methods

Beamtime at the BioMedical Imaging and Therapy (BMIT) beamline at the Canadian Light Source (CLS) was obtained through peer review under proposals 17-4996 and 18-5466. Animal ethics approval was granted under protocol 2012-0112 by the University of Saskatchewan Animal Research Ethics Board of the University Committee on Animal Care and Supply and by the Canadian Light Source.

3.3.1 Animals

Three male 8 week old Sprague-Dawley rats were used in this study. One animal was obtained *ex vivo* from a previous study (approved by the University of Saskatchewan Animal Research Ethics Board under protocol 2011-0124) where it had been used as a control animal for a study on the use of barium as an elemental tracker for new bone formation. The animals were purchased from Charles River and weighed 360 g and 381 g at the time they were scanned. The rats were housed in cages (16 × 27 × 42 cm), two animals per cage, at 20 °C with a light cycle of 12 h with access to food and water ad libitum.

3.3.2 Synchrotron ex vivo μCT

The BMIT 05B1-1 beamline is based off a 1.34T bending magnet x-ray source located within the 2.9 GeV storage ring at the CLS. The beam was prepared for imaging with a Bragg double crystal monochromator using Si (2, 2, 0) crystal reflections. The main imaging energy was 37 keV, located just above the k-edge of Barium, with comparison scans taken at 25 keV and 30 keV. This energy was used for easy applicability to other ongoing imaging projects. 37 keV is near the top end of the ability for imaging at BMIT, as the spectrum of the bend magnet drops off quickly, especially when monochromated (see figure 3.4 for details). Two detector set-ups were used: 1) a **C4742-98-ERG** Si CCD optical camera with a 1344 x 1024 array of 6.45 μm

x 6.45 µm pixels paired with an AA60 beam monitor P43 Gd_2O_2S:Tb 10µm thick scintillator, and 2) a **C4742-56-12HR** fiber optic window x-ray camera with a 2:1 FOP coupling of 10 µm fibers to a P43 Gd_2O_2S:Tb scintillator, resulting in a 4000 x 2624 array of 5.6 µm x 5.6 µm pixels (Hamamatsu, Hamamatsu City, Shizuoka Pref., Japan). Flat and dark field frames were collected before each scan to correct for noise in the detector and the x-ray beam. Pixel sizes in the projection images were 5 µm for the first camera without binning, 10 µm for the first detector with binning (2x2) and 11.8 µm for the second detector with binning (2x2). Specimens were scanned with exposure times ranging from 0.5-1.5s per frame, depending on the ring current, which decreases from a peak of 250 mA over time. Rotation steps of 0.24° and 0.5° were used to obtain 750 or 360 projection scans over 180°.

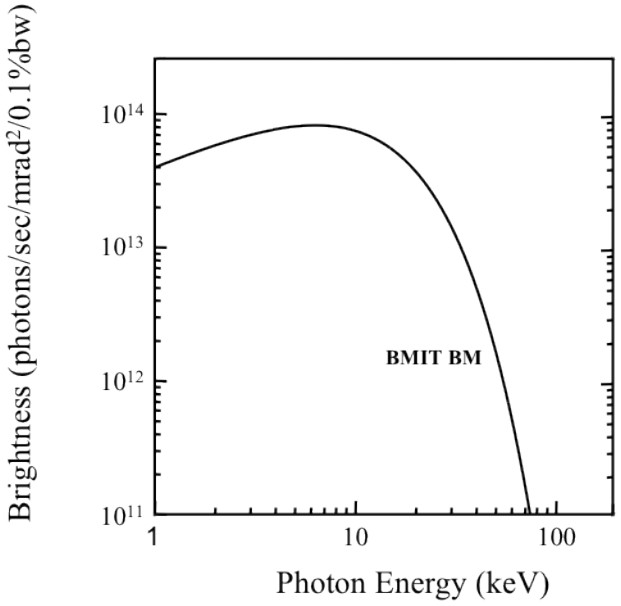

Figure 3.4: The x-ray source brightness for the BMIT bending magnet beam line, from 0 to 100 keV.

3.3.3 Ex vivo phase contrast setup and optimization

The front optical table at BMIT allows for a maximum distance from the sample to the detector of 1.2 m. Using an *ex vivo* forelimb tissue sample I captured a complete scan at 0.1m intervals to determine the optimal phase distance using both binning settings for the first camera and using the second camera. Once the phase distance is determined for a given set-up it can be directly translated from *ex vivo* to *in vivo* imaging without further configuration, so long as the energy and resolution remain the same.

3.3.5 Synchrotron in vivo μCT

The Hamamatsu C4742-56-12HR fiber optic window x-ray camera was used at the 11.2 μm resolution to scan two live Sprague-Dawley rats at 8 weeks of age. Slight divergence in the beam meant that the final spatial resolution was 11.8 μm. The direct fiber optic coupling in this detector system is up to 8-10 times more efficient than the lens based scintillator to CCD system used in the Hamamatsu C4742-98-ERG camera. The synchrotron x-ray beam was monochromated to 37.75 keV, a rotation step of 0.24 was used, leading to 750 projections. Aluminum filtration of 1.104 mm was used to eliminate any stray low energy harmonics. Due to lower ring current than normal at the CLS facility (a peak current of 145 mA compared to a normal peak of 250 mA), an exposure time of 1.2 s was used. A phase propagation distance of 0.9 m was used.

A custom built stage developed in collaboration with BMIT staff members (see figure 3.5) was used to fix the position of the forelimb in the path of the beam while holding the body of the animal steady and outside the imaging plane of the x-ray beam in order to reduce radiation exposure outside the target area. The stage also contains a place to attach a nose cone for gas anaesthetic. The animals were placed under isoflurane anaesthetic in an induction chamber under

the direction of the CLS veterinarian and their eyes were lubricated. They were then brought into the imaging hutch, where they were placed in the custom imaging stage and kept under anaesthesia using a nose cone until the end of the scan, at which point they were euthanized using an isoflurane overdose and exsanguinated. During the scan, the animals were monitored using CCTV video cameras, a pulse oximeter, a rectal thermometer, and their body temperature was maintained using a heat lamp. A fast shutter was used to stop the beam from irradiating the animals during the rotation of the stage between projections. During the scans, radiation exposure to the plane of the animals bodies was measured using luxel dosimeters (seen in figure 3.5 on the left) in use at the CLS to measure personnel radiation exposure. Stray radiation can result from scatter of the x-ray beam. In a final protocol, the animals can be protected from this by lead aprons or shields.

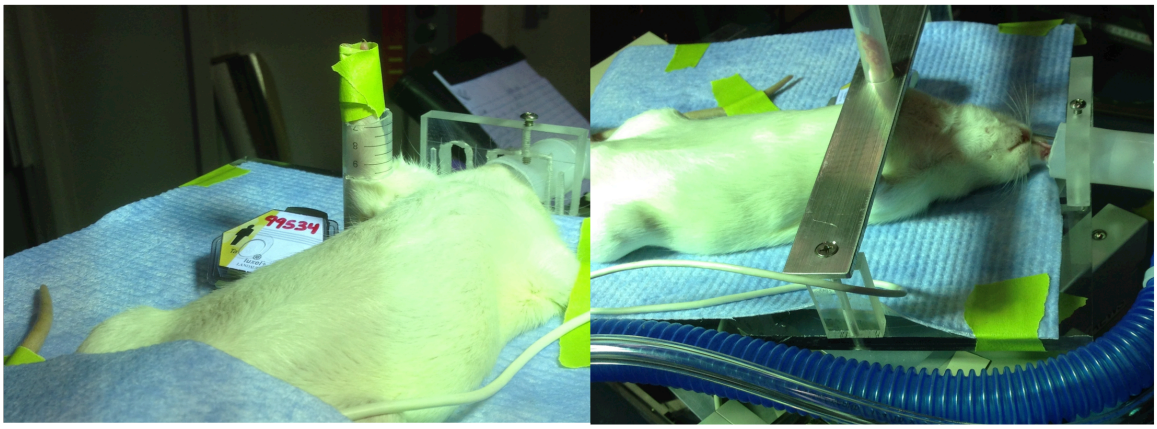

Figure 3.5: Rats positioned in the custom stage built at BMIT. On the left, a variant with the arm positioned in a tube in the beam. On the right, a variant with the arm held in a tube by a bridge.

Detector	Resolution	Voltage	Rotation step	Filter	Exposure time
C4742-98-ERG	5	37 keV	0.5, 0.24 °		500-1500 ms
C4742-98-ERG	10	25, 30, 37 keV	0.24 °		500-1500 ms
C4742-56-12HR	12	37.763 keV	0.24 °	1.104 mm Al	1200 ms

Table 3.1: Synchrotron µCT imaging protocols used

3.3.4 Desktop µCT

Comparative images were acquired in SkyScan 1076 and SkyScan 1176 (Bruker SkyScan, Kontich BE) desktop µCT systems. These scanners are designed for *in vivo* preclinical imaging of small animals such as mice, rats, and rabbits, and use a rotating gantry setup where the x-ray tube and detector pair rotate around the specimen. It is worth noting that the SkyScan 1176 is the newer model of the 1076 and possesses a higher power x-ray tube. The SkyScan 1076 contains a 10 W sealed x-ray tube capable of 20-100 kV, while the 1176 contains a 25 W sealed microfocus X-ray tube capable of 20-90 kV. The detectors used in the two scanners are capable of imaging with 9 µm, 18 µm, or 35 µm pixels. The SkyScan 1076 has the capacity for imaging at 9 µm however the time frame required for imaging is quite high at over an hour.

Six different imaging protocols were used and described as follows and summarized in Table 3.1 below. These different protocols are an attempt to capture the variety of settings commonly used for *in vivo* µCT imaging of trabecular bone. The 18µm protocols are currently used by groups doing *in vivo* µCT at the University of Alberta and elsewhere. The 9 µm protocols were chosen to capture the range of doses that could be produced by these systems at their highest resolution. All protocols followed the alignment of the systems and the capture of full sets of flat and dark images. In the SkyScan 1076, scans were performed at 18 µm with the x-ray tube set to 70 kV and 140 µA, using a 1.0 mm Aluminum filter, a 0.5 ° rotation step producing 360 projections, each with three frame-averaging, and an exposure time of 1.180 s. At 35 µm, scans were performed with the x-ray tube set to 70 kV and 140 µA, using a 0.5 mm Aluminum filter, a 0.5 ° rotation step producing 360 projections, each with three frame-averaging, and an exposure time of 0.474 s. In the SkyScan 1176, at 18 µm, scans were performed with the x-ray tube set to 70 kV and 287 µA, using a 1.0 mm Aluminum filter, a 0.5 °

rotation step producing 360 projections, each with three frame-averaging, and an exposure time of 0.350 s. At 9 μm, three different protocols were used to emphasize the ability of the system to produce drastically different radiation doses at the same resolution. In the 'low dose' protocol, the x-ray tube was set to 90 kV and 280 μA, using a 1.0 mm Aluminum filter, a 0.3 ° rotation step producing 600 projections, each with three frame-averaging, and an exposure time of 1.300 s. In the 'middle dose' protocol, the x-ray tube was set to 70 kV and 287 μA, using a 0.2 mm Aluminum filter, a 0.3 ° rotation step producing 600 projections, each with three frame-averaging, and an exposure time of 1.000 s. The high dose protocol used the x-ray tube set to 45 kV and 550 μA, using no metal filter, a 0.3 ° rotation step producing 600 projections, each with three frame-averaging, and an exposure time of 1.300 s.

A high resolution *ex vivo* protocol was also performed using a SkyScan 1172 model with a 10 W x-ray tube capable of 20-100 kV with a <5 μm spot size, which is able to detect isotropic details down to 0.7μm. The specimen was scanned at 6.5 μm, with 45 kV, 222 μA, a 0.15 rotation step producing 1200 projections, each with 4 frame averaging, and an exposure time of 200 ms.

System	Resolution	Voltage	Amperage	Rotation step	Filter	Exposure time	Frame averages
SkyScan 1076	35 µm	70 kV	140 µA	0.5 °	0.5 mm Al	474 ms	3
SkyScan 1076	18 µm	70 kV	140 µA	0.5 °	1.0 mm Al	1180 ms	3
SkyScan 1176	18 µm	70 kV	287 µA	0.5 °	1.0 mm Al	350 ms	3
SkyScan 1176 **'low dose'**	9 µm	90 kV	280 µA	0.3 °	1.0 mm Al	1300 ms	3
SkyScan 1176 **'medium dose'**	9 µm	70 kV	287 µA	0.3 °	0.2 mm Al	1000 ms	3
SkyScan 1176 **'high dose'**	9 µm	45 kV	550 µA	0.3 °	None	1300 ms	3
SkyScan 1172	6.5 µm	45 kV	222 µA	0.15 °	0.5 mm Al	200 ms	4

Table 3.2: Desktop µCT imaging protocols

3.3.6 Software

Projections obtained from synchrotron µCT were flat and dark corrected using a custom ImageJ (ImageJ, NIH) macro, and reconstructed using NRecon (Bruker SkyScan, Kontich BE), commercial software developed for use with SkyScan desktop µCT systems. Projections obtained from the SkyScan 1076 and 1176 models were corrected and reconstructed using NRecon directly. Data visualization was done using Amira (Visualization Sciences Group, Burlington Ma, USA), CTVox ((Bruker SkyScan, Kontich BE), and ImageJ.

3.3.7 Dosimetry

Lithium Fluoride (LiF) thermoluminescent dosimeters (TLDs) purchased from Mirion technologies (Mirion, Irvine Ca, USA) were used to measure the dose created by the synchrotron and desktop *ex vivo* protocols. Due to limited time and TLD availability either one or two LiF dosimeter devices were used for each scan. Each scan of a TLD chip dosimeter was performed using identical settings to the imaging protocols, with solely the TLD in the field of view.

Background radiation was corrected for using control crystals. The sensitivity of the TLD devices is 10 % as quoted from the commercial vender (Mirion). TLD chips have the advantage of small size and ease of use; however they are not always quickly available. As a result of time constraints, dosimetry for the synchrotron *in vivo* protocol was performed using a triad model Keithley 35050 ion chamber (Keithley Instruments, Inc., Cleveland, OH) calibrated for biomedical imaging. TLD dosimetry and this specific ion chamber model have been found to agree with an error rate of 2.5% (Figueroa et al. 2008). Luxel aluminum oxide (Al_2O_3) crystal OSL dosimeters were used in the in vivo phase to measure stray radiation impacted the animals bodies. Luxel dosimeter response was measured by Landauer (Landauer, Glenwood, IL).

3.4 Results

3.4.1 Resolution

Using the C4742-98-ERG camera I scanned at 5 μm and 10 μm to determine the resolution necessary to visualize the cortical porosity in the rat forelimb bones. 10 μm showed sufficient detail in the porosity and created at 10.0-10.8 Gy dose, and while using a 5 μm voxel size did improve the image quality, the resulting dose was much larger, at 25.6-35.1 Gy, than is tolerable for *in vivo* imaging in a small animal. See table 3.3 for details.

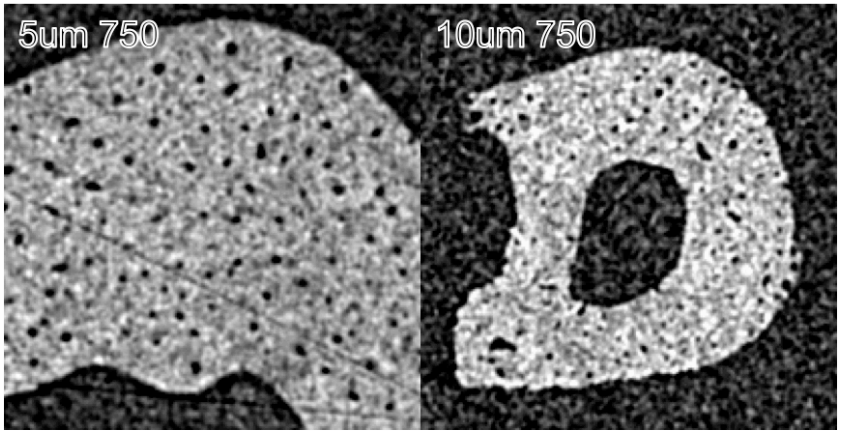

Figure 3.6: The difference between resolutions with 5 µm and 10 µm voxels using the C4742-98-ERG camera. The phase propagation distance for the 5 µm image is 0.3 m and for the 10 µm image is 0.6 m. Doses of 10.0-10.8 Gy were measured for the 10 µm protocol and 25.6-35.1 Gy for the 5 µm protocol.

3.4.2 Impact of number of projections

The number of projection images used to reconstruct the data set is a primary parameter in CT. Reducing the number used for reconstruction lowers the radiation dose but also reduces the resulting image quality due to a sparser sampling of image data. Higher numbers of projections tend to even out the image and reduce the noise levels within the data. I performed *ex vivo* µCT at BMIT and scanned the same sample at 360 projections and at 750 projections using the C4742-98-ERG camera to compare the resulting image quality, as shown in figure 3.6, with no frame averaging. Scanning with 360 projections resulted in images where the cortical porosity is visible but not able to be accurately segmented by a simple threshold.

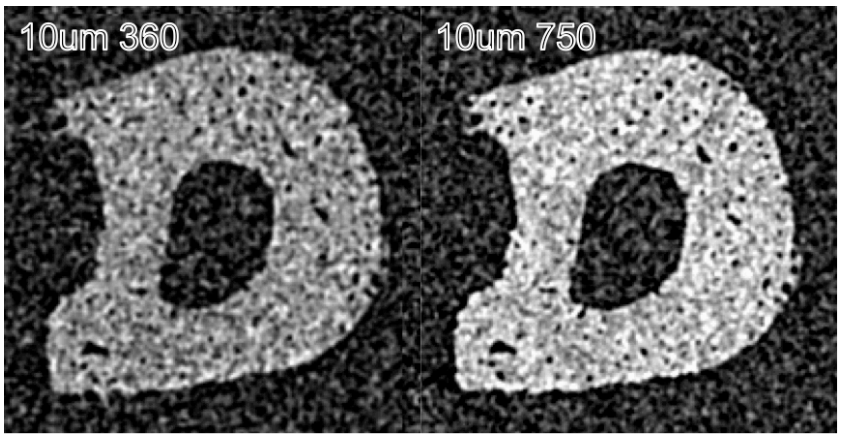

Figure 3.7: The impact of the number of projections on image quality can be seen, with a scan of 360 projections on the left compared to a scan of 750 projections on the right. These scans were performed with the C4742-98-ERG camera at 10 μm, and all other parameters were kept equal. Slice matches are not exact. Doses of 10.0-10.8 Gy were measured for this protocol.

3.4.2 Propagation distance

The propagation distance, between the object and the detector, is an important parameter for maximizing the image contrast obtained using in-line phase contrast μCT. Scanning at 0.1 m intervals I determined the optimal propagation distance for the C4742-98-ERG camera to be 0.6 m at 10 μm and 0.3 m at 5 μm, and for the C4742-56-12HR camera to be 0.9 m at 11.8 μm.

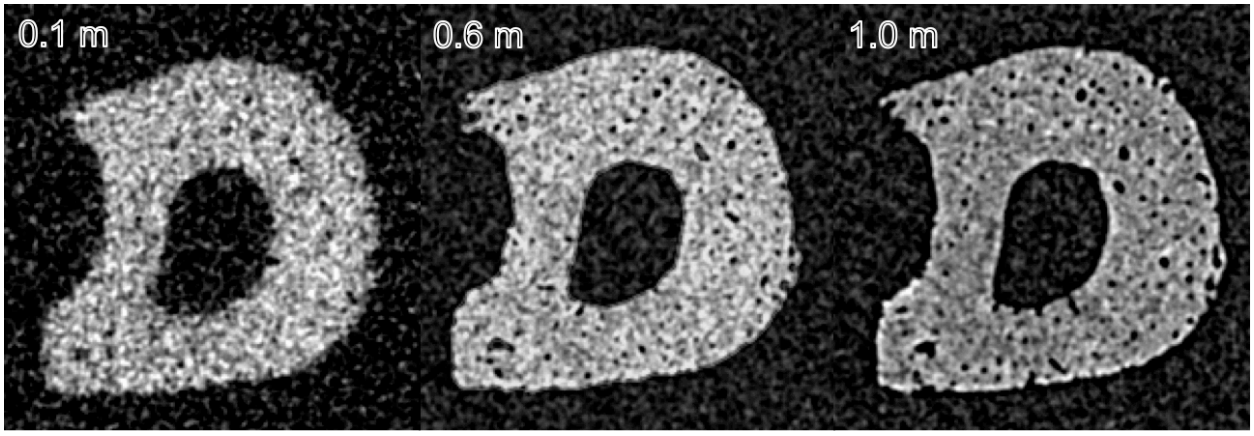

Figure 3.8: The optimal phase distance for the C4742-98-ERG camera at 10 μm was found to be 0.6 m. Selected propagation distances of 0.1 m, 0.6 m, and 1.0 m are shown for comparison. Slice matches are not exact. Doses of 10.0-10.8 Gy were measured for this protocol.

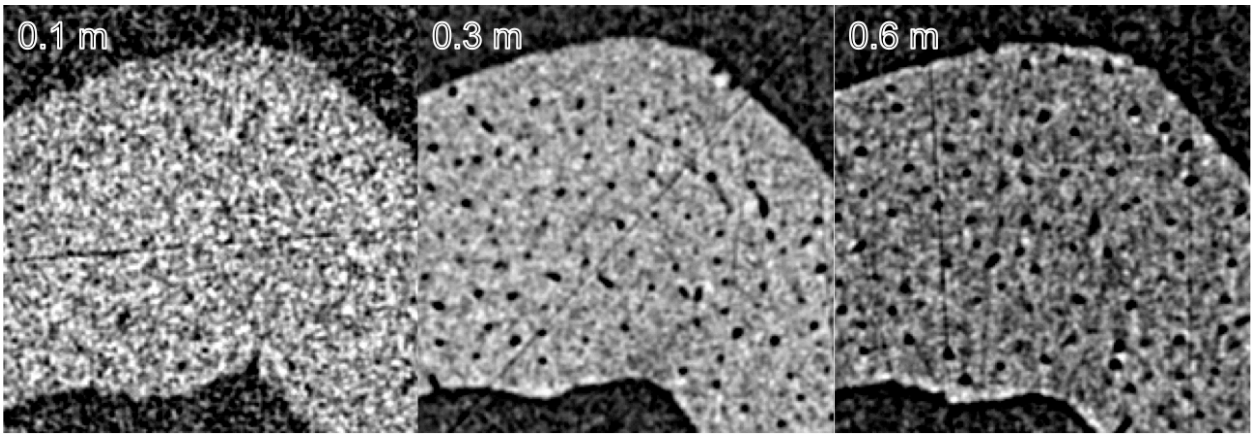

Figure 3.9: The optimal phase distance for the C4742-98-ERG camera at 5 μm was found to be 0.3 m. Selected propagation distances of 0.1 m, 0.6 m, and 0.6 m are shown for comparison. Slice matches are not exact. Doses of 25.6-35.1 Gy were measured for this protocol.

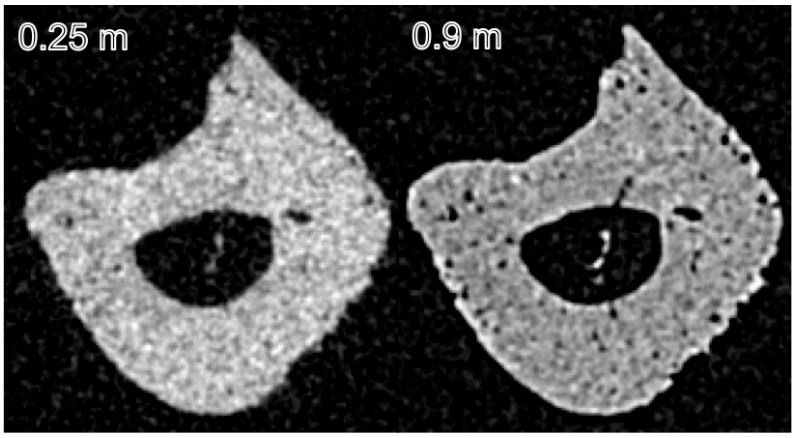

Figure 3.10: The optimal phase distance for the C4742-56-12HR camera was found to be 0.9 m. Selected propagation distances of 0.25 m, and 0.9 m are shown for comparison. Slice matches are not exact. A dose of 2.53 Gy was measured for this protocol.

3.4.3 Energy differences

Synchrotron scans at 25, 30, and 37 keV using the C4742-98-ERG camera at 10 μm with a phase distance of 0.6 m shows higher noise levels in the images taken at higher energy. The cortical porosity remains clearly visible and distinguishable from the phase contrast. The blurring in the lower energy images reflects that there are different optimal propagation distances at different x-ray energies, and in this case all three scans were taken using the optimal phase distance determined for 37 keV. Comparison images are shown in figure 3.11.

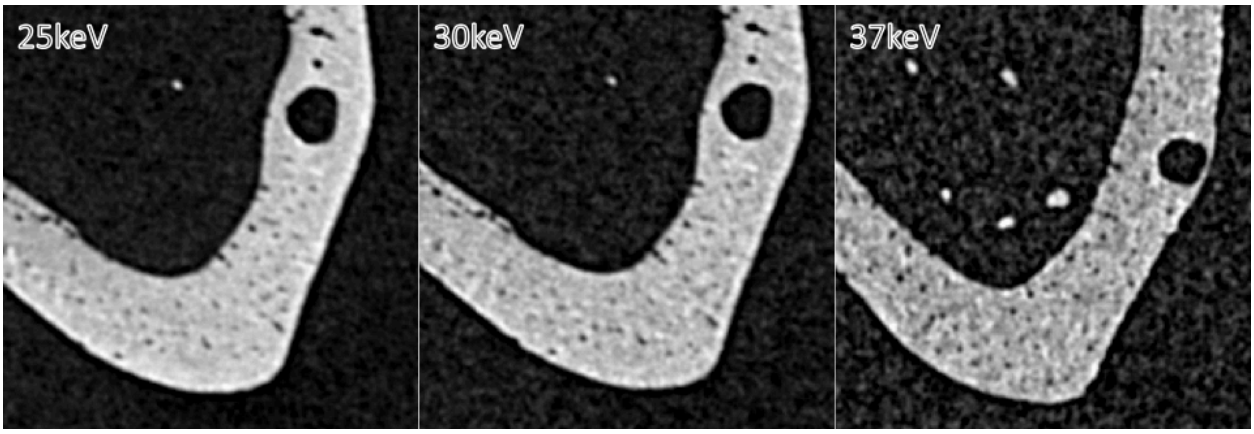

Figure 3.11: Differences in image quality using different x-ray energy in the tibia imaged using the C4742-98-ERG camera at 10 µm using a propagation distance of 0.6 m. Slice matches are not exact. Doses of 10.0-10.8 Gy were measured for this protocol.

3.4.4 dosimetry

Initial dosimetry for the *ex vivo* synchrotron µCT with the C4742-98-ERG camera at 10 µm created a dose of 10.0-10.8 Gy measured with TLD dosimetry. This precipitated a move to the C4742-56-12HR fibre optic camera. Using the Keithley ion chamber I calculated a dose of 3.2 Gy for the *ex vivo* preliminary tests and 2.5 Gy for the *in vivo* protocol. Using TLD dosimetry I obtained a dose of 1.2-1.5 Gy for the SkyScan 1176 µCT scanner at 18 µm, a dose of 3.2-3.6 for the SkyScan 1076 scanner at 18 µm, a dose of 11.7-54.2 Gy for the SkyScan 1176 scanner at 9 µm, depending on the protocol. Luxel dosimetry results indicated a minimal dose to the animal's bodies of 0.45 mGy and 1.67 mGy.

System	Protocol	Energy	Resolution	Dosimetry method	Dose
C4742-98-ERG	*Ex vivo*	37 keV	5 µm	TLD	25.6-35.1 Gy
C4742-98-ERG	*Ex vivo*	37 keV	10 µm	TLD	10.0-10.8 Gy
C4742-98-ERG	*Ex vivo*	30 keV	10 µm	TLD	13.7 Gy
C4742-98-ERG	*Ex vivo*	25 keV	10 µm	TLD	14.9 Gy
C4742-56-12HR	*Ex vivo*	37 keV	11.8 µm	Ion chamber	3.15 Gy
C4742-56-12HR	*In vivo*	37 keV	11.8 µm	Ion chamber	2.53 Gy
SkyScan 1076	*Ex vivo*	70 kV	18 µm	TLD	3.1-3.6 Gy
SkyScan 1176	*Ex vivo*	70 kV	18 µm	TLD	1.2-1.5 Gy
SkyScan 1176	*Ex vivo* – high dose	45 kV	9 µm	TLD	48.1-54.2 Gy
SkyScan 1176	*Ex vivo* – medium dose	70 kV	9 µm	TLD	18.6 Gy
SkyScan 1176	*Ex vivo* – low dose	90 kV	9 µm	TLD	11.7-18.2 Gy

Table 3.3: Measured doses for the different protocols

3.4.5 in vivo SR µCT

The right forelimb of two 8 week old Sprague-Dawley rats were imaged at BMIT using the C4742-56-12HR camera at 11.8 µm. The results of these scans indicate that movement during the scan is an issue, from blood flow and insufficient limb restriction. That said, the imaging was a success and the cortical porosity can be visualized, especially the larger targets including BMU related activity. A horizontal and longitudinal slice are shown in figures 3.12 and 3.13, with a volume render in figure 3.14.

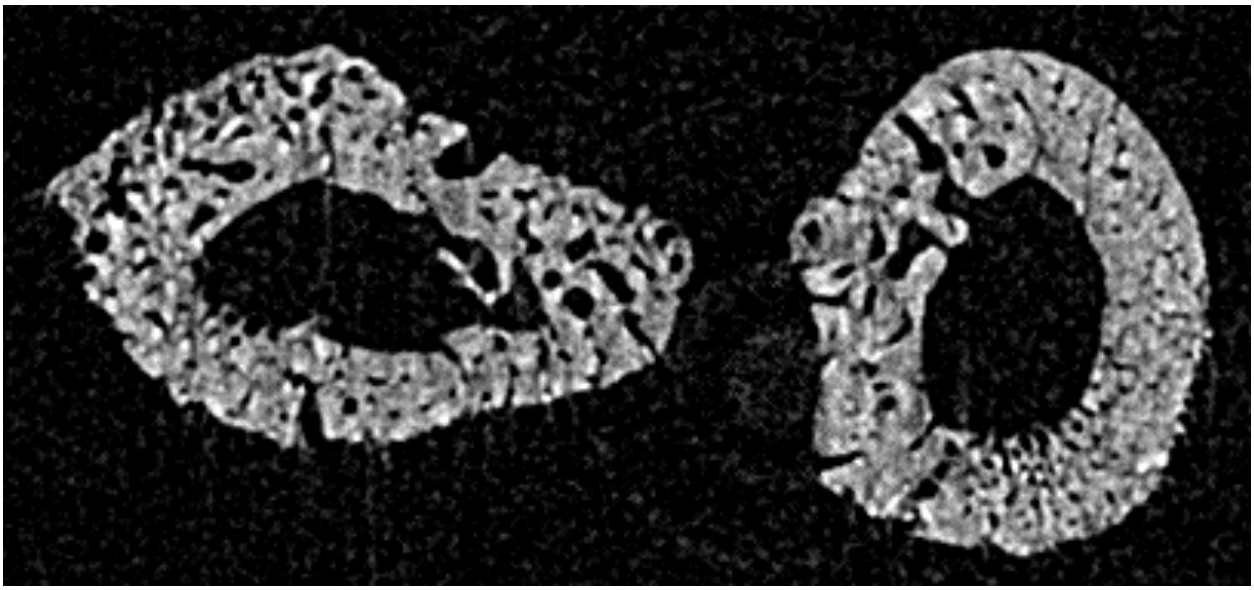

Figure 3.12: Single slice from the *in vivo* synchrotron μCT showing cortical porosity measured using the C4742-56-12HR camera at 11.8 μm with a 2.53 Gy dose.

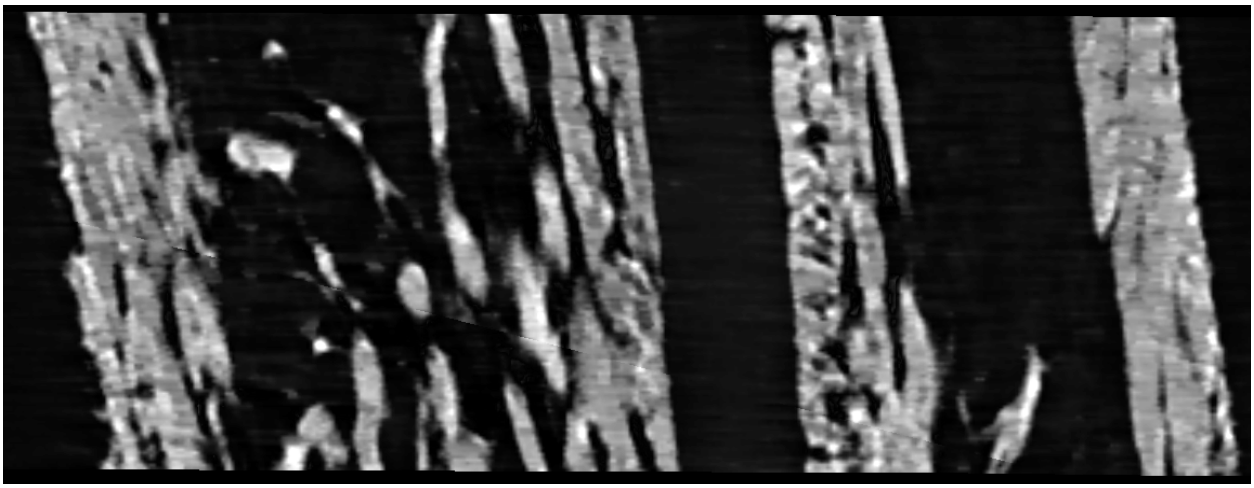

Figure 3.13: Longitudinal slice parallel to the long axis of the forelimb shows canals within the cortical bone, resliced in ImageJ from the *in vivo* scan using the C4742-56-12HR camera at 11.8 μm.

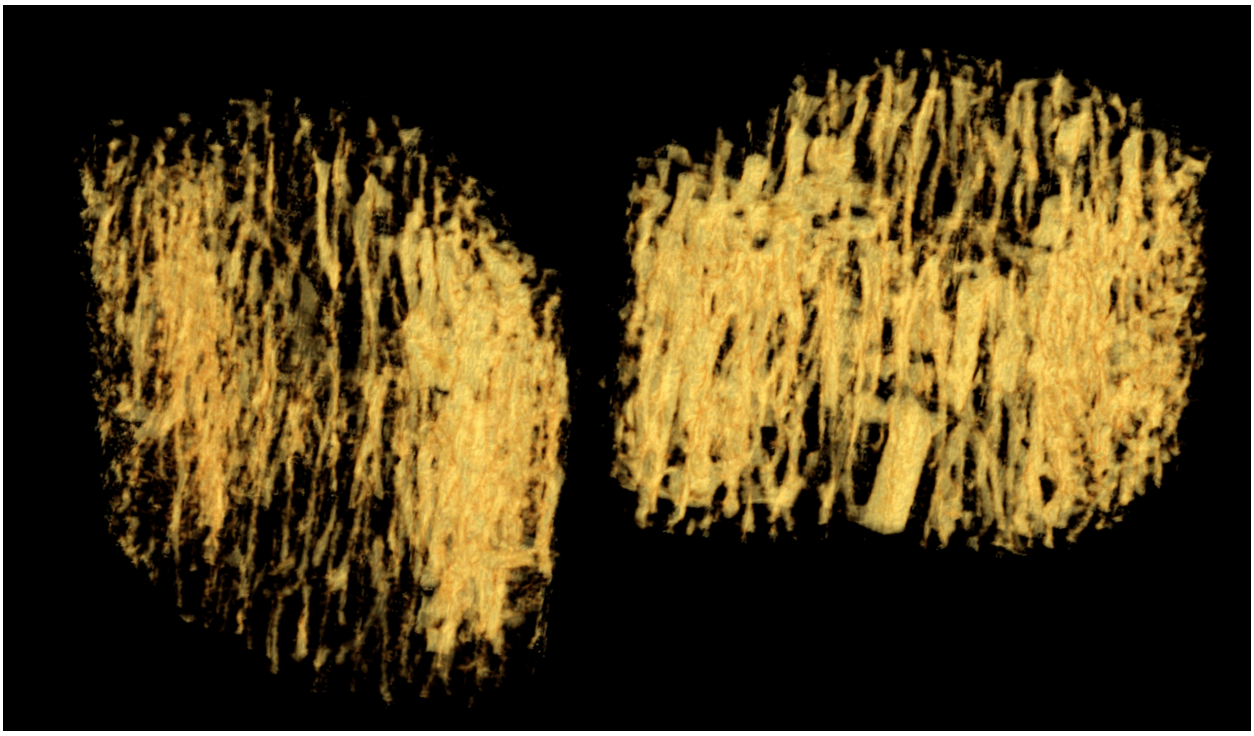

Figure 3.14: Volume render of the cortical porosity in the forelimb µCT scan

3.4.6 Comparison with desktop µCT

Comparison scans were done in SkyScan 1076 and 1176 *in vivo* µCT systems at 35 µm, 18 µm, and 9 µm. Comparative slices from these systems are shown in figure 3.15, 16, and 17, though the matches are not exact. The resolving power of these scans was below that of the *in vivo* synchrotron scans, even the desktop scan with 9 µm voxels. A SkyScan 1172 high resolution µCT system, designed for *ex vivo* scanning, was also used to perform a scan with 6.5 µm voxels, with the results shown in figure 3.18. The image quality for resolving the cortical porosity is on a similar level to the synchrotron *in vivo* scans done at 11.8 µm.

Figure 3:15: Slice reconstructed from the *in vivo* desktop SkyScan 1076 at 35 µm. Matching slice to the Synchrotron *in vivo*, any deviation is from positioning differences during the scans. Dose was not measured but is presumed to be lower than other scans.

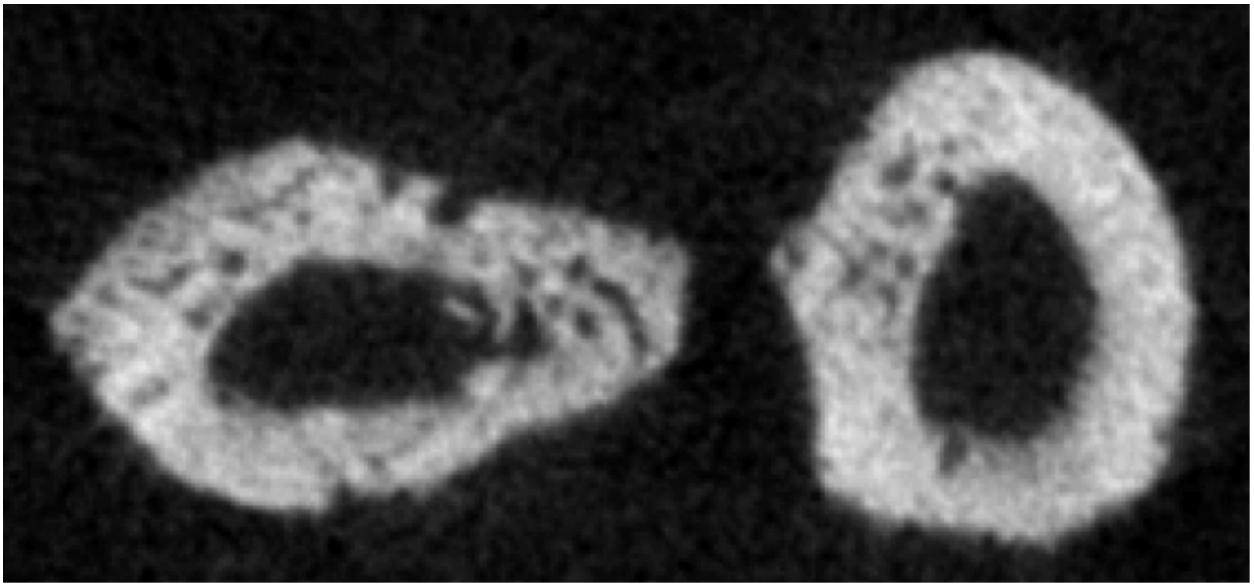

Figure 3:16: Slice reconstructed from the *in vivo* desktop SkyScan 1176 at 18 µm with a 1.2-1.5 Gy dose. Matching slice to the Synchrotron *in vivo*, any deviation is from positioning differences during the scans.

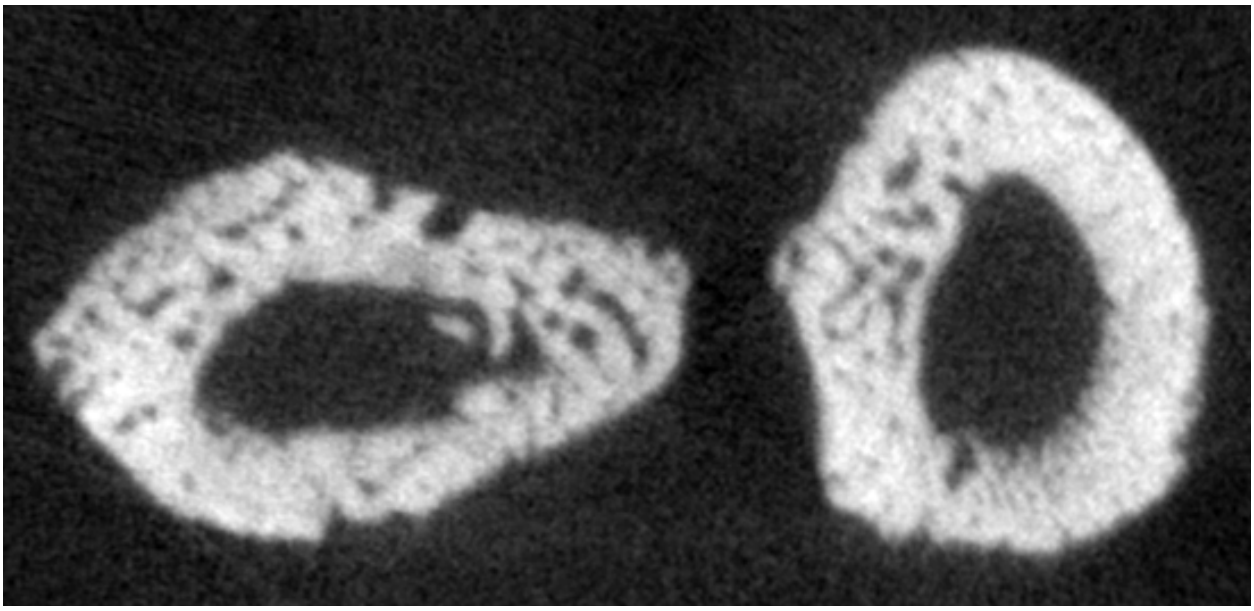

Figure 3:17: Slice reconstructed from the *in vivo* desktop SkyScan 1176 at 9 µm with an 11.7-18.2 Gy dose. Matching slice to the Synchrotron *in vivo*, any deviation is from positioning differences during the scans.

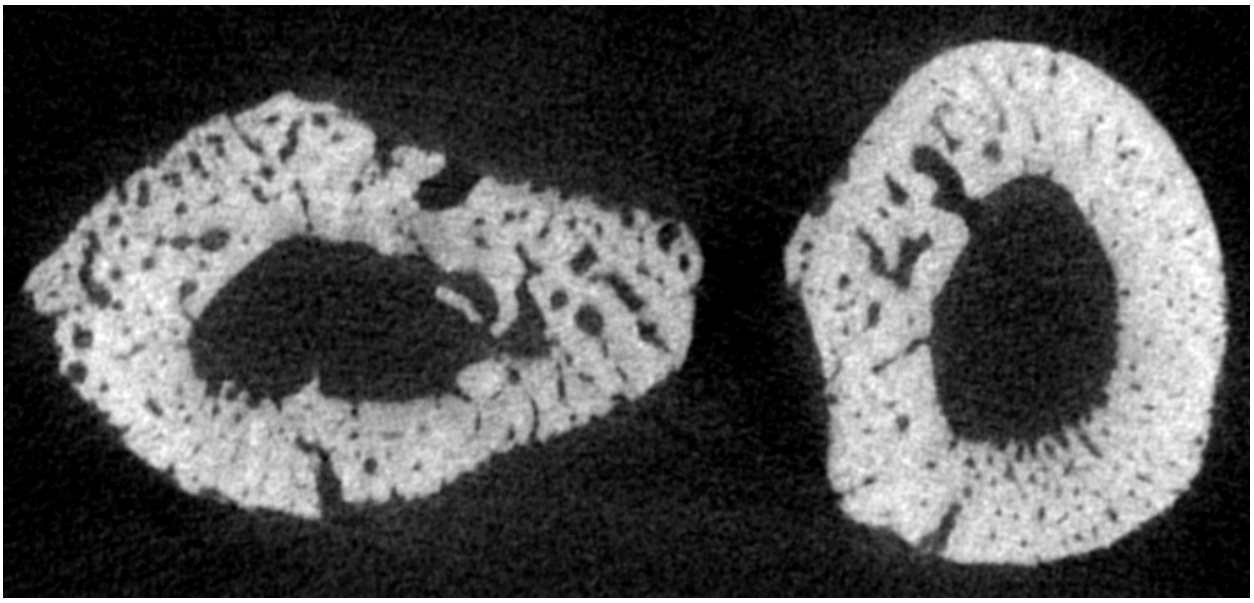

Figure 3.18: Slice reconstructed from the *ex vivo* desktop SkyScan 1172 at 6.5 µm. Matching slice to the Synchrotron *in vivo*, any deviation is from positioning differences during the scans. Dose was not measured but is presumed to be higher than other scans.

3.5 Discussion

Using the C4742-56-12HR camera at 11.8 μm, *in vivo* imaging of cortical porosity was achieved with a dose of 2.53 Gy, only slightly higher than doses used for *in vivo* analysis of trabecular bone. There are a number of future steps to be taken in order to lower the dose further. Technical limitations at the CLS and at BMIT meant that the camera readout time caused a delay in the imaging, and the ring current was lower than normal.

The number of projections is an important parameter in any approach to minimizing radiation dose to the animal. A change in the number of projections reflects a change in the x-ray exposure time to the animal, which is ultimately the most important parameter in the image quality. Any reduction in the time an animal spends in the beam, whether it is a reduction in exposure time, number of projections, or frame averaging, reduces the image quality, and the radiation dose. A reduction in one is often compensated for by an increase in the other parameters, and a balance must be found which best preserves the image quality. Signal to noise increases with the square root of the number of frames averaged (Webb 2003) so beyond 2-3 the parameter produces rapidly diminishing returns. Image quality at the centre of the reconstructed image is less reliant on larger numbers of projections, as the angular distance between projections is smaller towards the centre than at the outer edge of the image. New algorithms including iterative or compressed sensing approaches have potential to lower the number of projections required for imaging (Zhu et al. 2013) beyond what is possible with traditional filtered back projection reconstruction. In order to move beyond what is currently done with desktop *in vivo* μCT, parameters must be optimized before an increase in resolution can be attained.

The other option for reducing dose in the case when higher resolution is needed is imaging at higher x-ray energy. In a desktop μCT this means increasing the voltage, which will reduce the amperage that can be used and require longer exposure times to maintain contrast levels. In addition, higher energy x-rays produce lower contrast between similar tissue types, and are less suitable for measurements of mineral content. As can be seen in figures 3.8-3.10, noise levels within the bone are quite high which may throw off local measurements of bone mineral density. An initial assessment of the literature indicated that 5 μm resolution would be necessary for visualization of the cortical porosity (Matsumoto et al. 2006; Matsumoto et al. 2007). After imaging at 5 μm and 10 μm with the C4742-98-ERG camera, and at 11.8 μm with the C4742-56-12HR camera it appeared that the resolution provided by the 11.8 μm voxels still provided sufficient detail for cortical porosity visualization in the rats, likely due to the small spot size and precise collimation of the synchrotron beam along with the enhanced edge detection from the phase contrast. It is unlikely that this resolution would be sufficient to image cortical porosity in mice, as they have smaller cortical pores. See figure 3.12 as compared to figure 3.15-18: the desktop images are less noisy in the cortex, however, the level of porosity visible is lower except at the 6.5 μm resolution level. Dosimetry confirmed that imaging at 5 μm is likely unfeasible, with doses above 25 Gy. While I could likely have reduced that dose to the 10-15 Gy level by reducing the number of projections and the exposure time, the loss in image quality would produce images that are not suitable for data analysis.

The phase contrast makes a striking difference to the image quality, as shown in figures 3.8-3.10. In the absorption images, very little of the porosity is visible while in the optimized phase distance images the cortical porosity is obvious and striking. Part of the reason for the lack of contrast in the absorption image is likely the high energy used for the imaging. Synchrotron

bone imaging is commonly done at 25 keV, allowing excellent images of cortical and trabecular bone and local differences in mineralization. Imaging at the higher energy of 37 keV the radiation dose is reduced by nearly 40 % while the cortical porosity remains visible as shown in figure 3.11. It is well worth noting that the radiation dose in the absorption and the phase images is the same, providing a simple mechanism for lowering the radiation dose while improving the image quality. While 37 keV is near the limit of the BMIT bending magnet (BM) beamline, the BMIT insertion device (ID) beamline, based on a superconducting wiggler, will have an order of magnitude higher brilliance than the BM beamline and be able to image at energies up to 100 keV (see figure 3.19). This beamline is currently in commissioning status. The potential to image at 50 keV, just before the gadolinium k-edge (the fluorescent material in the scintillators I used), could further reduce the radiation dose by 46 % from the current imaging at 37 keV, bringing the current dose of 2.53 Gy down to a dose of 1.18 Gy, within the range of doses I measured for the desktop *in vivo* μCT protocols currently in use for trabecular bone imaging.

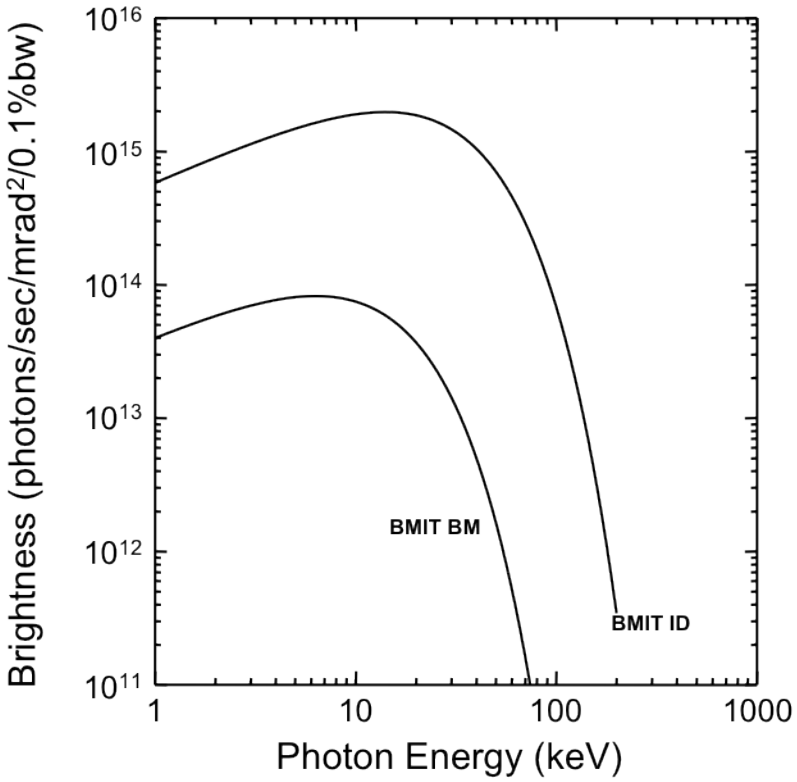

Figure 3.19: Brightness of the BMIT insertion device beamline compared to the BMIT bending magnet beamline.

The doses found for the desktop scanners were somewhat surprising and indicate what was previously noted: desktop "*in vivo*" scanners can create doses which are not tolerable to animals and which can easily affect the bone microarchitecture. Doses created by older scanners can be especially higher than expected. The doses created by the desktop protocol using the SkyScan 1076 at 18 μm were higher than the doses created by the synchrotron *in vivo* protocol at 11.8 μm. These protocols are in common use. Users should be cautious with the settings they choose, especially on older desktop μCT systems, as the doses created by these systems are limited only by their choices. The number of projections, and the frame averaging should be chosen so as to minimize dose, as settings that are high may be producing image quality that is better than required for trabecular architecture quantification. The doses produced by the desktop

system for imaging at 9 μm were excessively high, and although this resolution is provided by the system, it may be inadvisable for use on live animals, as doses will likely be above 10 Gy. The three protocols I created for use with the 9 μm voxel level all provided roughly equivalent image quality, while producing drastically different doses, from 11.7 to 54.2 Gy. From the dosimetry data collected, the radiation dose produced by the *in vivo* synchrotron protocol of 2.53 Gy falls within the range of desktop protocols at 18 μm, which produced doses from 1.2-3.6 Gy in the two desktop *in vivo* scanners.

3.6 Conclusions

Using the C4742-56-12HR camera at 11.8 μm, *in vivo* imaging of cortical porosity was achieved with a dose of 2.53 Gy. The use of propagation phase contrast enables a simple mechanism for dose reduction through high energy imaging. The dose created by the current synchrotron *in vivo* protocol is within the same order of magnitude as doses created by conventional desktop *in vivo* μCT, and future developments in technology will decrease that dose to levels within the range radiation doses created by common desktop μCT protocols.

It remains to be seen whether radiation doses of this level have effects on cortical bone microstructure, as previous studies have only examined the effect of dose on trabecular bone parameters. As well, data on the effect of dose on bone growth remains limited, especially with regards to the effects of dose in relation to the age and sex of the study animals. It is likely that younger animals with more metabolically active bone tissue will demonstrate effects from radiation at lower doses, potentially encouraging the use of older animals. However, older animals with less active tissue will respond less to experimental treatments, requiring potentially longer study periods with less chance of success. With that said, longitudinal imaging of cortical bone porosity using synchrotron phase contrast creates doses which are on the cusp of feasibility,

depending on further study of the effects of these slightly higher doses on cortical bone remodeling.

CHAPTER FOUR: CONCLUSION

Relative to the base of knowledge on the mechanisms of growth and development in trabecular microarchitecture, comparatively little is known about the processes of renewal and repair ongoing within cortical bone. The goal of this thesis was the development and preliminary implementation of a method for longitudinal 3D imaging of cortical porosity. Much of the knowledge regarding remodelling activity in cortical bone has come from histological studies, and it is only the recent availability of high resolution 3D imaging tools that has enabled development in this field. The resolution limitations of non x-ray based technologies preclude their use for cortical bone imaging, and the radiation dose caused by conventional μCT has thus far prevented its use in this area.

4.1 Overview

In chapter one the biological rationale for such a study was laid out and examined, and chapter two examined the current methodology in use for 3D bone imaging *in vivo*. It was found that current *in vivo* studies of bone using μCT are limited to trabecular bone analysis, as the radiation dose associated with high resolution cortical bone imaging is above the level shown to produce physiological effects on the scanned bone tissue.

Chapter three presented, to my knowledge, the first study to image the cortical bone canal network in living animals. Using high resolution propagation phase contrast synchrotron μCT at high energy, the cortical bone in the radius and ulna of a live rat was imaged using a C4742-56-12HR camera at 11.8 μm, with a dose of 2.53 Gy. The methodology for optimizing and implementing a scan of this nature was laid out, with particular emphasis on the resolution

required and the implementation of the phase contrast method. This study opens new possibilities for longitudinal imaging of cortical porosity and BMU related remodelling processes.

4.2 Future Directions

With this pilot study fully implemented, a large scale follow up study on the impacts and effects of this protocol is needed before experimental studies can progress. In particular, the effects of the radiation doses produced in the animal on cortical bone have not been quantified. Previous studies of radiation damage to bone have limited their focus to trabecular bone (Brouwers et al. 2007; Klinck et al. 2008; Laperre et al. 2011), as this has been the tissue under study. In this future study, it would be useful to scan animals at different dose levels, and examine the longitudinal effects of the imaging on the bone morphology. From such a study, the levels of safe imaging and the resulting image quality could be established as future longitudinal studies looking into structural growth processes in cortical bone need to be able to conclusively say that the effects seen are due to their experimental treatment and not to the effects of the radiation from the scans. Our group has planned a study examining the effects of two *in vivo* imaging sessions separated by two weeks. Groups of animals will be irradiated with doses of 1, 2, or 3 Gy per scan, and then followed up with higher resolution *ex vivo* μCT. Future technological development at BMIT includes the opening of the ID beamline for user access. The energy range on this beamline is 20-100 keV, and will allow higher energy imaging in less time. The current dose can be cut almost in half by increasing the x-ray energy from 37 keV to near 50 keV. The limitation at this high energy will be the detector response, which is known to decrease at higher energy.

One of the challenges for studies of cortical bone in small animals is the issue of remodelling. Rats do not normally undergo remodelling during life, but it can occur to mobilize calcium (Britz 2011) or as a response to damage in the bone (Noble et al. 2003). These mechanisms are exploited by a variety of different animal models to induce remodelling in rats or mice, by either increasing the loading regime, or increasing physiological demands for calcium. Different forms of exercise have been shown to induce cortical remodelling in rats (Notomi et al. 2000), and canal orientation changes depending on the loading regime present in the animals environment (Britz et al. 2012b). This model can be problematic as it is unclear whether it is the exercise itself which induces remodelling or whether the exercise is causing microdamage which is then causing the remodelling. This provides a confounding factor in studies on the relation of mechanical stimuli and remodelling as the BMU path will be altered by the creation of microcracks. In the second model, microcracks are induced deliberately through short periods of compressive loads placed on a limb, creating fatigue damage within the bone. This procedure has been shown to induce microcracks and remodelling; however, the exact mechanism for this process is as yet unknown (Macione et al. 2011; Mellon and Tanner 2012). The third model uses a methods to induce physiological mobilization of calcium, either a calcium restricted diet, an induced pregnancy followed by lactation, or a combination of the three (Medeiros et al. 2002). Remodeling in response to calcium restriction typically focuses on the endosteal surface, surrounding the medullary cavity, and is common as well in birds following egg laying (Bloom et al. 1941).

Using these different animal models, a variety of experimental studies can then be performed. Using longitudinal imaging of BMU related remodelling in cortical bone, the development of BMUs in bone can be tracked following fatigue loading, and following the

imaging protocol these bones can be histologically examined for signs of microcracks. By matching the histological slices and the *in vivo* μCT images, the progression of BMUs can be directly linked to the presence or absence of local microdamage, and the hypothesis that remodelling is steered towards microcracks can be tested. Specifically, the μCT imaging can locate the pre-existing BMUs and differentiate new growth and the direction of that growth after an experimental procedure, in this case the fatigue loading. There is no other technique that can visualize cortical porosity and BMUs in an *in vivo* animal model.

In addition to its use in laboratory animals such as mice and rats, questions involving larger animals can be examined as well. New Zealand white rabbits are a laboratory species which exhibit normal Haversian remodelling, and have potential for use in preclinical studies of drugs such as human parathyroid hormone (PTH), as well as estrogens, bisphosphonates, and other drugs which are known to affect bone structure and mass (Hirano et al. 1999). Longitudinal studies allow for direct testing of the effects of these drugs on cortical bone and the remodelling processes within, helping to elucidate the mechanisms by which these drugs act.

The orientation of BMUs and osteons in long bones has been linked to loading and through load history to the animals locomotor behaviour (Britz et al. 2012b; de Margerie 2002; de Margerie et al. 2005). The use of *in vivo* imaging at specific time points during the development of an animal's adult locomotor paradigm would allow for the measurement of direct change in the canal network and its relation to mechanical loading and behaviour. If such a link were established, it could allow researchers to look into the past and potentially determine new information about the locomotor behaviours of animals long extinct, or of human ancestors, adding to the knowledge provided by trabecular bone studies (Fajardo and Müller 2001; Fajardo et al. 2007; Griffin et al. 2010; Ryan and Shaw 2012; Sanchez et al. 2012).

4.3 Conclusion

This thesis has laid the ground work for an effective μCT protocol for imaging cortical bone porosity and BMU related remodeling in living animals using synchrotron propagation phase contrast. I have demonstrated that neurovascular canals within rat cortical bone can be visualized and quantified in 3D using phase contrast μCT, and while it is not possible to differentiate primary and secondary canals *in vivo*, the progression of canals will be traceable over time. The information gained from this study will inform a larger scale study on the effects of dose on remodeling, as well as experimental studies on remodeling in living animals. The ability to track the progression of individual BMUs over time cannot be underestimated for its importance in the creation of a fuller knowledge of the processes of renewal and repair in bone tissues.

REFERENCES

Ammann P, and Rizzoli R. 2003. Bone strength and its determinants. Osteoporosis international : a journal established as result of cooperation between the European Foundation for Osteoporosis and the National Osteoporosis Foundation of the USA 14 Suppl 3:S13-18.

Andrews JC, Almeida E, van der Meulen MC, Alwood JS, Lee C, Liu Y, Chen J, Meirer F, Feser M, Gelb J et al. . 2010. Nanoscale X-ray microscopic imaging of mammalian mineralized tissue. Microscopy and microanalysis : the official journal of Microscopy Society of America, Microbeam Analysis Society, Microscopical Society of Canada 16(3):327-336.

Arhatari BD, Cooper DM, Thomas CD, Clement JG, and Peele AG. 2011. Imaging the 3D structure of secondary osteons in human cortical bone using phase-retrieval tomography. Physics in medicine and biology 56(16):5265-5274.

Barak MM, Lieberman DE, and Hublin JJ. 2013. Of mice, rats and men: Trabecular bone architecture in mammals scales to body mass with negative allometry. Journal of structural biology.

Basillais A, Bensamoun S, Chappard C, Brunet-Imbault B, Lemineur G, Ilharreborde B, Ho Ba Tho MC, and Benhamou CL. 2007. Three-dimensional characterization of cortical bone microstructure by microcomputed tomography: validation with ultrasonic and microscopic measurements. Journal of orthopaedic science : official journal of the Japanese Orthopaedic Association 12(2):141-148.

Bayat S, Apostol L, Boller E, Brochard T, and Peyrin F. 2005. In vivo imaging of bone micro-architecture in mice with 3D synchrotron radiation micro-tomography. Nucl Instrum Meth A 548(1-2):247-252.

Bentolila V, Boyce T, Fyhrie D, Drumb R, Skerry T, and Schaffler M. 1998. Intracortical remodeling in adult rat long bones after fatigue loading. Bone 23(3):275-281.

Betz O, Wegst U, Weide D, Heethoff M, Helfen L, Lee WK, and Cloetens P. 2007. Imaging applications of synchrotron X-ray phase-contrast microtomography in biological morphology and biomaterials science. 1. General aspects of the technique and its advantages in the analysis of millimetre-sized arthropod structure. J Microsc-Oxford 227(1):51-71.

Bisgard JD, and Hunt HB. 1936. Influence of Roentgen Rays and Radium on Epiphyseal Growth of Long Bones. Radiology 26(1):56-68.

Bloom W, Bloom MA, and McLean FC. 1941. Calcification and ossification. Medullary bone changes in the reproductive cycle of female pigeons. The Anatomical record 81(4):443-475.

Boone JM. 2007. The trouble with CTD100. Medical physics 34(4):1364-1371.

Boone JM, Velazquez O, and Cherry SR. 2004. Small-animal X-ray dose from micro-CT. Molecular imaging 3(3):149-158.

Borah B, Dufresne T, Nurre J, Phipps R, Chmielewski P, Wagner L, Lundy M, Bouxsein M, Zebaze R, and Seeman E. 2010. Risedronate reduces intracortical porosity in women with osteoporosis. Journal of bone and mineral research : the official journal of the American Society for Bone and Mineral Research 25(1):41-47.

Borah B, Gross GJ, Dufresne TE, Smith TS, Cockman MD, Chmielewski PA, Lundy MW, Hartke JR, and Sod EW. 2001. Three-dimensional microimaging (MRmicroI and microCT), finite element modeling, and rapid prototyping provide unique insights into bone architecture in osteoporosis. The Anatomical record 265(2):101-110.

Bos AJJ. 2001. High sensitivity thermoluminescence dosimetry. Nucl Instrum Meth B 184(1-2):3-28.

Boutroy S, Bouxsein ML, Munoz F, and Delmas PD. 2005. In vivo assessment of trabecular bone microarchitecture by high-resolution peripheral quantitative computed tomography. The Journal of clinical endocrinology and metabolism 90(12):6508-6515.

Bouxsein ML, Boyd SK, Christiansen BA, Guldberg RE, Jepsen KJ, and Muller R. 2010. Guidelines for assessment of bone microstructure in rodents using micro-computed tomography. Journal of bone and mineral research : the official journal of the American Society for Bone and Mineral Research 25(7):1468-1486.

Boyd SK. 2008. Site-specific variation of bone micro-architecture in the distal radius and tibia. Journal of clinical densitometry : the official journal of the International Society for Clinical Densitometry 11(3):424-430.

Boyd SK, Davison P, Muller R, and Gasser JA. 2006a. Monitoring individual morphological changes over time in ovariectomized rats by in vivo micro-computed tomography. Bone 39(4):854-862.

Boyd SK, Moser S, Kuhn M, Klinck RJ, Krauze PL, Musser R, and Gasser JS. 2006b. Evaluation of three-dimensional image registration methodologies for in vivo micro-computed tomography. Ann Biomed Eng 34(10):1587-1599.

Britz HM. 2011. The development of a small animal model for assessing the 3D implications of loading on bone microarchitecture.

Britz HM, Carter Y, Jokihaara J, Leppanen OV, Jarvinen TL, Belev G, and Cooper DM. 2012a. Prolonged unloading in growing rats reduces cortical osteocyte lacunar density and volume in the distal tibia. Bone 51(5):913-919.

Britz HM, Jokihaara J, Leppanen OV, Jarvinen T, and Cooper DM. 2010. 3D visualization and quantification of rat cortical bone porosity using a desktop micro-CT system: a case study in the tibia. Journal of microscopy 240(1):32-37.

Britz HM, Jokihaara J, Leppanen OV, Jarvinen TL, and Cooper DM. 2012b. The effects of immobilization on vascular canal orientation in rat cortical bone. Journal of anatomy 220(1):67-76.

Brouwers JE, van Rietbergen B, and Huiskes R. 2007. No effects of in vivo micro-CT radiation on structural parameters and bone marrow cells in proximal tibia of wistar rats detected after eight weekly scans. Journal of orthopaedic research : official publication of the Orthopaedic Research Society 25(10):1325-1332.

Bruker S. 2012. Morphometric parameters measured by Skyscan CT- analyser software.

Buie HR, Campbell GM, Klinck RJ, MacNeil JA, and Boyd SK. 2007. Automatic segmentation of cortical and trabecular compartments based on a dual threshold technique for in vivo micro-CT bone analysis. Bone 41(4):505-515.

Burger EH, Klein-Nulend J, and Smit TH. 2003. Strain-derived canalicular fluid flow regulates osteoclast activity in a remodelling osteon--a proposal. Journal of biomechanics 36(10):1453-1459.

Burr DB, Martin RB, Schaffler MB, and Radin EL. 1985. Bone remodeling in response to in vivo fatigue microdamage. Journal of biomechanics 18(3):189-200.

Bushberg JT. 2002. The essential physics of medical imaging. Philadelphia: Lippincott Williams & Wilkins. xvi, 933 p. p.

Campbell GM, Ominsky MS, and Boyd SK. 2011. Bone quality is partially recovered after the discontinuation of RANKL administration in rats by increased bone mass on existing

trabeculae: an in vivo micro-CT study. Osteoporosis international : a journal established as result of cooperation between the European Foundation for Osteoporosis and the National Osteoporosis Foundation of the USA 22(3):931-942.

Carter DR. 1984. Mechanical loading histories and cortical bone remodeling. Calcified tissue international 36(1):S19-S24.

Carter Y, Thomas CD, Clement JG, Peele AG, Hannah K, and Cooper DM. 2013. Variation in osteocyte lacunar morphology and density in the human femur--a synchrotron radiation micro-CT study. Bone 52(1):126-132.

Chapman D, Thomlinson W, Johnston RE, Washburn D, Pisano E, Gmur N, Zhong Z, Menk R, Arfelli F, and Sayers D. 1997. Diffraction enhanced x-ray imaging. Physics in medicine and biology 42(11):2015-2025.

Chappard D, Legrand E, Haettich B, Chales G, Auvinet B, Eschard JP, Hamelin JP, Basle MF, and Audran M. 2001. Fractal dimension of trabecular bone: comparison of three histomorphometric computed techniques for measuring the architectural two-dimensional complexity. The Journal of pathology 195(4):515-521.

Chen H, Zhou X, Shoumura S, Emura S, and Bunai Y. 2010. Age- and gender-dependent changes in three-dimensional microstructure of cortical and trabecular bone at the human femoral neck. Osteoporosis international : a journal established as result of cooperation between the European Foundation for Osteoporosis and the National Osteoporosis Foundation of the USA 21(4):627-636.

Choi CH, Kim HT, Choe JY, Kim SK, Choi GW, Jheon S, and Kim JK. 2010. In vivo high-resolution synchrotron radiation imaging of collagen-induced arthritis in a rodent model. Journal of synchrotron radiation 17(3):393-399.

Coan P, Bamberg F, Diemoz PC, Bravin A, Timpert K, Mutzel E, Raya JG, Adam-Neumair S, Reiser MF, and Glaser C. 2010a. Characterization of osteoarthritic and normal human patella cartilage by computed tomography X-ray phase-contrast imaging: a feasibility study. Investigative radiology 45(7):437-444.

Coan P, Wagner A, Bravin A, Diemoz PC, Keyrilainen J, and Mollenhauer J. 2010b. In vivo x-ray phase contrast analyzer-based imaging for longitudinal osteoarthritis studies in guinea pigs. Physics in medicine and biology 55(24):7649-7662.

Cooper D, Turinsky A, Sensen C, and Hallgrimsson B. 2007a. Effect of voxel size on 3D micro-CT analysis of cortical bone porosity. Calcified tissue international 80(3):211-219.

Cooper DM, Bewer B, Wiebe S, Wysokinski TW, and Chapman D. 2011a. Diffraction enhanced X-ray imaging of the distal radius: a novel approach for visualization of trabecular bone architecture. Canadian Association of Radiologists journal = Journal l'Association canadienne des radiologistes 62(4):251-255.

Cooper DM, Erickson B, Peele AG, Hannah K, Thomas CD, and Clement JG. 2011b. Visualization of 3D osteon morphology by synchrotron radiation micro-CT. Journal of anatomy 219(4):481-489.

Cooper DM, Matyas JR, Katzenberg MA, and Hallgrimsson B. 2004. Comparison of microcomputed tomographic and microradiographic measurements of cortical bone porosity. Calcified tissue international 74(5):437-447.

Cooper DM, Thomas CD, Clement JG, and Hallgrimsson B. 2006. Three-dimensional microcomputed tomography imaging of basic multicellular unit-related resorption spaces in human cortical bone. The anatomical record Part A, Discoveries in molecular, cellular, and evolutionary biology 288(7):806-816.

Cooper DM, Thomas CD, Clement JG, Turinsky AL, Sensen CW, and Hallgrimsson B. 2007b. Age-dependent change in the 3D structure of cortical porosity at the human femoral midshaft. Bone 40(4):957-965.

Cooper DM, Turinsky AL, Sensen CW, and Hallgrimsson B. 2003. Quantitative 3D analysis of the canal network in cortical bone by micro-computed tomography. Anatomical record Part B, New anatomist 274(1):169-179.

Currey JD. 2002. Bones : structure and mechanics. Princeton, NJ: Princeton University Press.

Dare A, Hachisu R, Yamaguchi A, Yokose S, Yoshiki S, and Okano T. 1997. Effects of ionizing radiation on proliferation and differentiation of osteoblast-like cells. Journal of dental research 76(2):658-664.

David C, Nohammer B, Solak HH, and Ziegler E. 2002. Differential x-ray phase contrast imaging using a shearing interferometer. Appl Phys Lett 81(17):3287-3289.

David V, Laroche N, Boudignon B, Lafage-Proust MH, Alexandre C, Ruegsegger P, and Vico L. 2003. Noninvasive in vivo monitoring of bone architecture alterations in hindlimb-unloaded female rats using novel three-dimensional microcomputed tomography. Journal of bone and mineral research : the official journal of the American Society for Bone and Mineral Research 18(9):1622-1631.

de Margerie E. 2002. Laminar bone as an adaptation to torsional loads in flapping flight. Journal of anatomy 201(6):521-526.

de Margerie E, Sanchez S, Cubo J, and Castanet J. 2005. Torsional resistance as a principal component of the structural design of long bones: comparative multivariate evidence in birds. The anatomical record Part A, Discoveries in molecular, cellular, and evolutionary biology 282(1):49-66.

Dehoff RT. 1983. Quantitative Serial Sectioning Analysis - Preview. J Microsc-Oxford 131(Sep):259-263.

Dempster DW, Compston JE, Drezner MK, Glorieux FH, Kanis JA, Malluche H, Meunier PJ, Ott SM, Recker RR, and Parfitt AM. 2013. Standardized nomenclature, symbols, and units for bone histomorphometry: a 2012 update of the report of the ASBMR Histomorphometry Nomenclature Committee. Journal of bone and mineral research : the official journal of the American Society for Bone and Mineral Research 28(1):2-17.

Donath T, Pfeiffer F, Bunk O, Grünzweig C, Hempel E, Popescu S, Vock P, and David C. 2010. Toward clinical X-ray phase-contrast CT: demonstration of enhanced soft-tissue contrast in human specimen. Investigative radiology 45(7):445-452.

Dudziak ME, Saadeh PB, Mehrara BJ, Steinbrech DS, Greenwald JA, Gittes GK, and Longaker MT. 2000. The effects of ionizing radiation on osteoblast-like cells in vitro. Plastic and reconstructive surgery 106(5):1049-1061.

Duncan RL, and Turner CH. 1995. Mechanotransduction and the functional response of bone to mechanical strain. Calcified tissue international 57(5):344-358.

Eames BF, Allen N, Young J, Kaplan A, Helms JA, and Schneider RA. 2007. Skeletogenesis in the swell shark Cephaloscyllium ventriosum. Journal of anatomy 210(5):542-554.

Eriksen EF. 2010. Cellular mechanisms of bone remodeling. Reviews in endocrine & metabolic disorders 11(4):219-227.

Fajardo R, and Müller R. 2001. Three−dimensional analysis of nonhuman primate trabecular architecture using micro−computed tomography. American journal of physical anthropology 115(4):327-336.

Fajardo RJ, Müller R, Ketcham RA, and Colbert M. 2007. Nonhuman anthropoid primate femoral neck trabecular architecture and its relationship to locomotor mode. The Anatomical record 290(4):422-436.

Feldkamp LA, Goldstein SA, Parfitt AM, Jesion G, and Kleerekoper M. 1989. The Direct Examination of 3-Dimensional Bone Architecture Invitro by Computed-Tomography. Journal of Bone and Mineral Research 4(1):3-11.

Figueroa SD, Winkelmann CT, Miller HW, Volkert WA, and Hoffman TJ. 2008. TLD assessment of mouse dosimetry during microCT imaging. Medical physics 35(9):3866-3874.

Ford NL, Thornton MM, and Holdsworth DW. 2003. Fundamental image quality limits for microcomputed tomography in small animals. Medical physics 30(11):2869-2877.

Freidberg W, Copeland K, Duke FE, O'Brien K, and Darden EB. 1999. Guidelines and technical information provided by the us federal aviation administration to promote radiation safety for air carrier crew members. Radiat Prot Dosim 86(4):323-327.

Frost HM. 1958. Preparation of thin undecalcified bone sections by rapid manual method. Stain technology 33(6):273-277.

Frost HM. 1963. Bone remodelling dynamics. Springfield, Ill.,: Thomas. 175 p. p.

Frost HM. 1987. Bone "mass" and the "mechanostat": a proposal. The Anatomical record 219(1):1-9.

Gal TJ, Munoz-Antonia T, Muro-Cacho CA, and Klotch DW. 2000. Radiation effects on osteoblasts in vitro: a potential role in osteoradionecrosis. Archives of otolaryngology--head & neck surgery 126(9):1124-1128.

Griffin NL, D'Août K, Ryan TM, Richmond BG, Ketcham RA, and Postnov A. 2010. Comparative forefoot trabecular bone architecture in extant hominids. Journal of human evolution 59(2):202-213.

Hasnah MO, Zhong Z, Oltulu O, Pisano E, Johnston RE, Sayers D, Thomlinson W, and Chapman D. 2002. Diffraction enhanced imaging contrast mechanisms in breast cancer specimens. Medical physics 29(10):2216-2221.

Hert J, Fiala P, and Petrtyl M. 1994. Osteon orientation of the diaphysis of the long bones in man. Bone 15(3):269-277.

Hildebrand T, Laib A, Muller R, Dequeker J, and Ruegsegger P. 1999. Direct three-dimensional morphometric analysis of human cancellous bone: microstructural data from spine, femur, iliac crest, and calcaneus. Journal of bone and mineral research : the official journal of the American Society for Bone and Mineral Research 14(7):1167-1174.

Hildebrand T, and Ruegsegger P. 1997a. A new method for the model-independent assessment of thickness in three-dimensional images. J Microsc-Oxford 185:67-75.

Hildebrand T, and Ruegsegger P. 1997b. Quantification of Bone Microarchitecture with the Structure Model Index. Computer methods in biomechanics and biomedical engineering 1(1):15-23.

Hirano T, Burr DB, Turner CH, Sato M, Cain RL, and Hock JM. 1999. Anabolic effects of human biosynthetic parathyroid hormone fragment (1–34), LY333334, on remodeling and mechanical properties of cortical bone in rabbits. Journal of bone and Mineral Research 14(4):536-545.

Hounsfield GN. 1973. Computerized transverse axial scanning (tomography). 1. Description of system. The British journal of radiology 46(552):1016-1022.

Huang W, Yang Y, Sun Z, and Zeng X. 2009. Early radiation-induced bone marrow injury: serial MR imaging during initial 4 weeks after irradiation. Academic radiology 16(6):733-738.

Iliakis G, Wang Y, Guan J, and Wang H. 2003. DNA damage checkpoint control in cells exposed to ionizing radiation. Oncogene 22(37):5834-5847.

Izadifar Z, Chapman D, and Chen D. 2013. Computed tomography diffraction enhanced imaging for in situ visualization of tissue scaffolds implanted in cartilage. Tissue engineering Part C, Methods.

Jacobsson M, Jonsson A, Albrektsson T, and Turesson I. 1985. Alterations in bone regenerative capacity after low level gamma irradiation. A quantitative study. Scandinavian journal of plastic and reconstructive surgery 19(3):231-236.

Jast J, and Jasiuk I. 2013. Age-related changes in the 3D hierarchical structure of rat tibia cortical bone characterized by high resolution micro-CT. J Appl Physiol.

Jowsey J. 1966. Studies of Haversian systems in man and some animals. Journal of anatomy 100(Pt 4):857-864.

Kabel J, Odgaard A, van Rietbergen B, and Huiskes R. 1999. Connectivity and the elastic properties of cancellous bone. Bone 24(2):115-120.

Kinney JH, Lane N, Majumdar S, Marshall SJ, and Marshall GW. 1992. Noninvasive, 3-Dimensional Histomorphometry Using X-Ray Tomographic Microscopy. Journal of Bone and Mineral Research 7:S136-S136.

Kinney JH, Lane NE, and Haupt DL. 1995. In vivo, three-dimensional microscopy of trabecular bone. Journal of bone and mineral research : the official journal of the American Society for Bone and Mineral Research 10(2):264-270.

Kinney JH, Ryaby JT, Haupt DL, and Lane NE. 1998. Three-dimensional in vivo morphometry of trabecular bone in the OVX rat model of osteoporosis. Technology and health care : official journal of the European Society for Engineering and Medicine 6(5-6):339-350.

Klinck RJ, Campbell GM, and Boyd SK. 2008. Radiation effects on bone architecture in mice and rats resulting from in vivo micro-computed tomography scanning. Medical engineering & physics 30(7):888-895.

Koch JC. 1917. The laws of bone architecture. American Journal of Anatomy 21(2):177-298.

Kohlbrenner A, Hammerle S, Laib A, and Ruegsegger P. 2000. A 3D microtomographic system with stacked fan-beam geometry. Nucl Instrum Meth A 443(2-3):531-539.

Kohlbrenner A, Koller B, Hammerle S, and Ruegsegger P. 2001. In vivo micro tomography. Advances in experimental medicine and biology 496:213-224.

Kotre CJ, and Birch IP. 1999. Phase contrast enhancement of x-ray mammography: a design study. Physics in medicine and biology 44(11):2853-2866.

Krug R, Carballido-Gamio J, Burghardt AJ, Kazakia G, Hyun BH, Jobke B, Banerjee S, Huber M, Link TM, and Majumdar S. 2008. Assessment of trabecular bone structure comparing magnetic resonance imaging at 3 Tesla with high-resolution peripheral quantitative computed tomography ex vivo and in vivo. Osteoporosis international : a journal established as result of cooperation between the European Foundation for Osteoporosis and the National Osteoporosis Foundation of the USA 19(5):653-661.

Kubo T, Shiga T, Hashimoto J, Yoshioka M, Honjo H, Urabe M, Kitajima I, Semba I, and Hirasawa Y. 1999. Osteoporosis influences the late period of fracture healing in a rat model prepared by ovariectomy and low calcium diet. The Journal of steroid biochemistry and molecular biology 68(5):197-202.

Lak M, Neraudeau D, Nel A, Cloetens P, Perrichot V, and Tafforeau P. 2008. Phase contrast X-ray synchrotron imaging: Opening access to fossil inclusions in opaque amber. Microscopy and Microanalysis 14(3):251-259.

Lambers FM, Kuhn G, Schulte FA, Koch K, and Muller R. 2012. Longitudinal assessment of in vivo bone dynamics in a mouse tail model of postmenopausal osteoporosis. Calcified tissue international 90(2):108-119.

Lambers FM, Schulte FA, Kuhn G, Webster DJ, and Muller R. 2011. Mouse tail vertebrae adapt to cyclic mechanical loading by increasing bone formation rate and decreasing bone resorption rate as shown by time-lapsed in vivo imaging of dynamic bone morphometry. Bone 49(6):1340-1350.

Lane NE, Haupt D, Kimmel DB, Modin G, and Kinney JH. 1999. Early estrogen replacement therapy reverses the rapid loss of trabecular bone volume and prevents further deterioration of connectivity in the rat. Journal of bone and mineral research : the official journal of the American Society for Bone and Mineral Research 14(2):206-214.

Lane NE, Kumer J, Yao W, Breunig T, Wronski T, Modin G, and Kinney JH. 2003. Basic fibroblast growth factor forms new trabeculae that physically connect with pre-existing trabeculae, and this new bone is maintained with an anti-resorptive agent and enhanced with an anabolic agent in an osteopenic rat model. Osteoporosis international : a journal established as result of cooperation between the European Foundation for Osteoporosis and the National Osteoporosis Foundation of the USA 14(5):374-382.

Lane NE, Thompson JM, Haupt D, Kimmel DB, Modin G, and Kinney JH. 1998. Acute changes in trabecular bone connectivity and osteoclast activity in the ovariectomized rat in vivo.

Journal of bone and mineral research : the official journal of the American Society for Bone and Mineral Research 13(2):229-236.

Langer M, Pacureanu A, Suhonen H, Grimal Q, Cloetens P, and Peyrin F. 2012. X-ray phase nanotomography resolves the 3D human bone ultrastructure. PloS one 7(8):e35691.

Laperre K, Depypere M, van Gastel N, Torrekens S, Moermans K, Bogaerts R, Maes F, and Carmeliet G. 2011. Development of micro-CT protocols for in vivo follow-up of mouse bone architecture without major radiation side effects. Bone 49(4):613-622.

Lewis RA. 2004. Medical phase contrast x-ray imaging: current status and future prospects. Physics in medicine and biology 49(16):3573-3583.

Lieben L, Benn B, Ajibade D, Stockmans I, Moermans K, Hediger M, Peng J, Christakos S, Bouillon R, and Carmeliet G. 2010. Trpv6 mediates intestinal calcium absorption during calcium restriction and contributes to bone homeostasis. Bone 47(2):301-308.

Lieberman DE, Polk JD, and Demes B. 2004. Predicting long bone loading from cross-sectional geometry. American journal of physical anthropology 123(2):156-171.

Macione J, Kavukcuoglu NB, Nesbitt RS, Mann AB, Guzelsu N, and Kotha SP. 2011. Hierarchies of damage induced loss of mechanical properties in calcified bone after in vivo fatigue loading of rat ulnae. Journal of the mechanical behavior of biomedical materials 4(6):841-848.

Martin RB. 2002. Is all cortical bone remodeling initiated by microdamage? Bone 30(1):8-13.

Martin RB. 2007. Targeted bone remodeling involves BMU steering as well as activation. Bone 40(6):1574-1580.

Matsumoto T, Nishikawa K, Tanaka M, and Uesugi K. 2011. In vivo CT quantification of trabecular bone dynamics in mice after sciatic neurectomy using monochromatic synchrotron radiation. Calcified tissue international 88(5):432-441.

Matsumoto T, Yoshino M, Asano T, Uesugi K, Todoh M, and Tanaka M. 2006. Monochromatic synchrotron radiation muCT reveals disuse-mediated canal network rarefaction in cortical bone of growing rat tibiae. J Appl Physiol 100(1):274-280.

Matsumoto T, Yoshino M, Uesugi K, and Tanaka M. 2007. Biphasic change and disuse-mediated regression of canal network structure in cortical bone of growing rats. Bone 41(2):239-246.

Matsumura S, Jikko A, Hiranuma H, Deguchi A, and Fuchihata H. 1996. Effect of X-ray irradiation on proliferation and differentiation of osteoblast. Calcified tissue international 59(4):307-308.

McCollough CH, Leng S, Yu L, Cody DD, Boone JM, and McNitt-Gray MF. 2011. CT dose index and patient dose: they are not the same thing. Radiology 259(2):311-316.

Medeiros DM, Plattner A, Jennings D, and Stoecker B. 2002. Bone morphology, strength and density are compromised in iron-deficient rats and exacerbated by calcium restriction. The Journal of nutrition 132(10):3135-3141.

Mellon S, and Tanner K. 2012. Bone and its adaptation to mechanical loading: a review. International Materials Reviews 57(5):235-255.

Mitchell MJ, and Logan PM. 1998. Radiation-induced changes in bone. Radiographics : a review publication of the Radiological Society of North America, Inc 18(5):1125-1136; quiz 1242-1123.

Mollenhauer J, Aurich ME, Zhong Z, Muehleman C, Cole AA, Hasnah M, Oltulu O, Kuettner KE, Margulis A, and Chapman LD. 2002. Diffraction-enhanced X-ray imaging of articular cartilage. Osteoarthritis and cartilage / OARS, Osteoarthritis Research Society 10(3):163-171.

Momose A, Takeda T, and Itai Y. 2000. Blood vessels: depiction at phase-contrast X-ray imaging without contrast agents in the mouse and rat-feasibility study. Radiology 217(2):593-596.

Momose A, Takeda T, Itai Y, and Hirano K. 1996. Phase-contrast X-ray computed tomography for observing biological soft tissues. Nature medicine 2(4):473-475.

Muller R, and Ruegsegger P. 1995. Three-dimensional finite element modelling of non-invasively assessed trabecular bone structures. Medical engineering & physics 17(2):126-133.

Nishiyama KK, Campbell GM, Klinck RJ, and Boyd SK. 2010. Reproducibility of bone micro-architecture measurements in rodents by in vivo micro-computed tomography is maximized with three-dimensional image registration. Bone 46(1):155-161.

Noble BS, Peet N, Stevens HY, Brabbs A, Mosley JR, Reilly GC, Reeve J, Skerry TM, and Lanyon LE. 2003. Mechanical loading: biphasic osteocyte survival and targeting of osteoclasts for bone destruction in rat cortical bone. American journal of physiology Cell physiology 284(4):C934-943.

Notomi T, Lee SJ, Okimoto N, Okazaki Y, Takamoto T, Nakamura T, and Suzuki M. 2000. Effects of resistance exercise training on mass, strength, and turnover of bone in growing rats. European journal of applied physiology 82(4):268-274.

Odgaard A. 1997. Three-dimensional methods for quantification of cancellous bone architecture. Bone 20(4):315-328.

Odgaard A, Andersen K, Melsen F, and Gundersen HJ. 1990. A direct method for fast three-dimensional serial reconstruction. Journal of microscopy 159(Pt 3):335-342.

Odgaard A, and Gundersen HJ. 1993. Quantification of connectivity in cancellous bone, with special emphasis on 3-D reconstructions. Bone 14(2):173-182.

Olive PL, Banath JP, and Durand RE. 1990. Heterogeneity in radiation-induced DNA damage and repair in tumor and normal cells measured using the "comet" assay. Radiation research 122(1):86-94.

Parfitt AM. 1984. Age-related structural changes in trabecular and cortical bone: cellular mechanisms and biomechanical consequences. Calcified tissue international 36 Suppl 1:S123-128.

Parfitt AM, Drezner MK, Glorieux FH, Kanis JA, Malluche H, Meunier PJ, Ott SM, and Recker RR. 1987. Bone histomorphometry: standardization of nomenclature, symbols, and units. Report of the ASBMR Histomorphometry Nomenclature Committee. Journal of bone and mineral research : the official journal of the American Society for Bone and Mineral Research 2(6):595-610.

Particelli F, Mecozzi L, Beraudi A, Montesi M, Baruffaldi F, and Viceconti M. 2012. A comparison between micro-CT and histology for the evaluation of cortical bone: effect of polymethylmethacrylate embedding on structural parameters. Journal of microscopy 245(3):302-310.

Paulus MJ, Sari-Sarraf H, Gleason SS, Bobrek M, Hicks JS, Johnson DK, Behel JK, Thompson LH, and Allen WC. 1999. A new X-ray computed tomography system for laboratory mouse imaging. Ieee T Nucl Sci 46(3):558-564.

Pauwels B, Bruyndonckx P, Liu X, Tapfer A, Velroyen A, Yaroshenko A, Bech M, Pfeiffer F, and Sasov A. 2012. First small-animal in-vivo phase-contrast micro-CT scanner. SPIE Optical Engineering+ Applications: International Society for Optics and Photonics. p 85060J-85060J-85068.

Pearson OM, and Lieberman DE. 2004. The aging of Wolff's "law": ontogeny and responses to mechanical loading in cortical bone. American journal of physical anthropology Suppl 39:63-99.

Perilli E, Le V, Ma B, Salmon P, Reynolds K, and Fazzalari NL. 2010. Detecting early bone changes using in vivo micro-CT in ovariectomized, zoledronic acid-treated, and sham-operated rats. Osteoporosis international : a journal established as result of cooperation between the European Foundation for Osteoporosis and the National Osteoporosis Foundation of the USA 21(8):1371-1382.

Petrtyl M, Hert J, and Fiala P. 1996. Spatial organization of the haversian bone in man. Journal of biomechanics 29(2):161-169.

Peyrin F. 2009. Investigation of bone with synchrotron radiation imaging: from micro to nano. Osteoporosis Int 20(6):1057-1063.

Peyrin F, Salome M, Cloetens P, Laval-Jeantet AM, Ritman E, and Ruegsegger P. 1998. Micro-CT examinations of trabecular bone samples at different resolutions: 14, 7 and 2 micron level. Technology and health care : official journal of the European Society for Engineering and Medicine 6(5-6):391-401.

Pfeiffer F, Bech M, Bunk O, Kraft P, Eikenberry EF, Bronnimann C, Grunzweig C, and David C. 2008. Hard-X-ray dark-field imaging using a grating interferometer. Nature materials 7(2):134-137.

Pisano ED, Johnston RE, Chapman D, Geradts J, Iacocca MV, Livasy CA, Washburn DB, Sayers DE, Zhong Z, Kiss MZ et al. . 2000. Human breast cancer specimens: diffraction-enhanced imaging with histologic correlation--improved conspicuity of lesion detail compared with digital radiography. Radiology 214(3):895-901.

Reimann DA, Hames SM, Flynn MJ, and Fyhrie DP. 1997. A cone beam computed tomography system for true 3D imaging of specimens. Applied radiation and isotopes : including data, instrumentation and methods for use in agriculture, industry and medicine 48(10-12):1433-1436.

Robling AG, Castillo AB, and Turner CH. 2006. Biomechanical and molecular regulation of bone remodeling. Annual review of biomedical engineering 8:455-498.

Ruegsegger P, Kohlbrenner A, Ulrich D, and Laib A. 1999. First results of a multiple fan-beam approach to analyze bone structure in vivo. P Soc Photo-Opt Ins 3772:55-62.

Ryan TM, and Shaw CN. 2012. Unique suites of trabecular bone features characterize locomotor behavior in human and non-human anthropoid primates. PloS one 7(7):e41037.

Sanchez S, Ahlberg PE, Trinajstic KM, Mirone A, and Tafforeau P. 2012. Three-Dimensional Synchrotron Virtual Paleohistology: A New Insight into the World of Fossil Bone Microstructures. Microscopy and Microanalysis 18(5):1095.

Santos A, Bakker AD, and Klein-Nulend J. 2009. The role of osteocytes in bone mechanotransduction. Osteoporosis international : a journal established as result of

cooperation between the European Foundation for Osteoporosis and the National Osteoporosis Foundation of the USA 20(6):1027-1031.

Sasov A. 2002. In-vivo micro-CT for small animals imaging. 2002 Ieee International Symposium on Biomedical Imaging, Proceedings:377-380.

Sasov A, and Dewaele D. 2002. High-resolution in-vivo micro-CT scanner for small animals. Developments in X-Ray Tomography Iii 4503:256-264.

Sassov A, and Van Dyck D. 2000. Phase-contrast microtomography with polychromatic sealed source. Aip Conf Proc 507:521-524.

Scheven BA, Burger EH, Kawilarang-de Haas EW, Wassenaar AM, and Nijweide PJ. 1985. Effects of ionizing irradiation on formation and resorbing activity of osteoclasts in vitro. Laboratory investigation; a journal of technical methods and pathology 53(1):72-79.

Schneider P, Stauber M, Voide R, Stampanoni M, Donahue LR, and Muller R. 2007. Ultrastructural properties in cortical bone vary greatly in two inbred strains of mice as assessed by synchrotron light based micro- and nano-CT. Journal of bone and mineral research : the official journal of the American Society for Bone and Mineral Research 22(10):1557-1570.

Schulte FA, Lambers FM, Kuhn G, and Muller R. 2011. In vivo micro-computed tomography allows direct three-dimensional quantification of both bone formation and bone resorption parameters using time-lapsed imaging. Bone 48(3):433-442.

Seeman E. 2002. Pathogenesis of bone fragility in women and men. Lancet 359(9320):1841-1850.

Seeman E. 2004. The growth and age-related origins of bone fragility in men. Calcified tissue international 75(2):100-109.

Shope TB, Gagne RM, and Johnson GC. 1981. A method for describing the doses delivered by transmission x-ray computed tomography. Medical physics 8(4):488-495.

Smith TM, Tafforeau P, Reid DJ, Grun R, Egginsll S, Boutakiout M, and Hublin JJ. 2007. Earliest evidence of modern human life history in North African early Homo sapiens. Proceedings of the National Academy of Sciences of the United States of America 104(15):6128-6133.

Smith TM, Tafforeauc P, Reid DJ, Pouech J, Lazzari V, Zermeno JP, Guatelli-Steinberg D, Olejniczak AJ, Hoffman A, Radovcic J et al. . 2010. Dental evidence for ontogenetic differences between modern humans and Neanderthals. Proceedings of the National Academy of Sciences of the United States of America 107(49):20923-20928.

Snigirev A, Snigireva I, Kohn V, Kuznetsov S, and Schelokov I. 1995. On the possibilities of x−ray phase contrast microimaging by coherent high−energy synchrotron radiation. Review of Scientific Instruments 66(12):5486-5492.

Tafforeau P, Boistel R, Boller E, Bravin A, Brunet M, Chaimanee Y, Cloetens P, Feist M, Hoszowska J, Jaeger JJ et al. . 2006. Applications of X-ray synchrotron microtomography for non-destructive 3D studies of paleontological specimens. Appl Phys a-Mater 83(2):195-202.

Tapfer A, Braren R, Bech M, Willner M, Zanette I, Weitkamp T, Trajkovic-Arsic M, Siveke JT, Settles M, Aichler M et al. . 2013. X-Ray Phase-Contrast CT of a Pancreatic Ductal Adenocarcinoma Mouse Model. PloS one 8(3):e58439.

United Nations. Scientific Committee on the Effects of Atomic Radiation. 2010. Sources and effects of ionizing radiation : United Nations Scientific Committee on the Effects of

Atomic Radiation : UNSCEAR 2008 report to the General Assembly, with scientific annexes. New York: United Nations.

Voide R, Schneider P, Stauber M, Wyss P, Stampanoni M, Sennhauser U, van Lenthe GH, and Muller R. 2009. Time-lapsed assessment of microcrack initiation and propagation in murine cortical bone at submicrometer resolution. Bone 45(2):164-173.

Waarsing JH, Day JS, van der Linden JC, Ederveen AG, Spanjers C, De Clerck N, Sasov A, Verhaar JA, and Weinans H. 2004a. Detecting and tracking local changes in the tibiae of individual rats: a novel method to analyse longitudinal in vivo micro-CT data. Bone 34(1):163-169.

Waarsing JH, Day JS, and Weinans H. 2004b. An improved segmentation method for in vivo microCT imaging. Journal of bone and mineral research : the official journal of the American Society for Bone and Mineral Research 19(10):1640-1650.

Wachter NJ, Augat P, Krischak GD, Sarkar MR, Mentzel M, Kinzl L, and Claes L. 2001. Prediction of strength of cortical bone in vitro by microcomputed tomography. Clin Biomech (Bristol, Avon) 16(3):252-256.

Webb AR. 2003. Introduction to biomedical imaging. Hoboken, New Jersey: Wiley. xiii, 252 p. p.

Weinbaum S, Cowin SC, and Zeng Y. 1994. A model for the excitation of osteocytes by mechanical loading-induced bone fluid shear stresses. Journal of biomechanics 27(3):339-360.

Wilkins S, Gureyev T, Gao D, Pogany A, and Stevenson A. 1996. Phase-contrast imaging using polychromatic hard X-rays. Nature 384(6607):335-338.

Willey JS, Lloyd SA, Robbins ME, Bourland JD, Smith-Sielicki H, Bowman LC, Norrdin RW, and Bateman TA. 2008. Early increase in osteoclast number in mice after whole-body irradiation with 2 Gy X rays. Radiation research 170(3):388-392.

Yu C, and Luxton G. 1999. TLD dose measurement: A simplified accurate technique for the dose range from 0.5 cGy to 1000 cGy. Medical physics 26(6):1010-1016.

Yukihara EG, Mardirossian G, Mirzasadeghi M, Guduru S, and Ahmad S. 2008. Evaluation of Al2O3:C optically stimulated luminescence (OSL) dosimeters for passive dosimetry of high-energy photon and electron beams in radiotherapy. Medical physics 35(1):260-269.

Yukihara EG, and McKeever SW. 2008. Optically stimulated luminescence (OSL) dosimetry in medicine. Physics in medicine and biology 53(20):R351-379.

Zhou SA, and Brahme A. 2008. Development of phase-contrast X-ray imaging techniques and potential medical applications. Phys Med 24(3):129-148.

Zhu N, Chapman D, Cooper D, Schreyer DJ, and Chen X. 2011. X-ray diffraction enhanced imaging as a novel method to visualize low-density scaffolds in soft tissue engineering. Tissue engineering Part C, Methods 17(11):1071-1080.

Zhu Z, Wahid K, Babyn P, Cooper D, Pratt I, and Carter Y. 2013. Improved Compressed Sensing-Based Algorithm for Sparse-View CT Image Reconstruction. Computational and Mathematical Methods in Medicine 2013:15.

APPENDIX A: ETHICS APPROVAL

UNIVERSITY OF SASKATCHEWAN

Animal Research Ethics Board (AREB)

Certificate of Approval

PRINCIPAL INVESTIGATOR	DEPARTMENT/ORGANIZATION	ANIMAL USE PROTOCOL #
Dr. David Cooper	Anatomy & Cell Biology	20110124

TITLE
Pilot study to identify barium deposition in bone of a rat model through high resolution imaging

SPONSORING AGENCIES
Canada Foundation for Innovation

BIOSAFETY NUMBER
ANA-14

UNIFI FUND #

APPROVAL DATE:	APPROVAL OF:	EXPIRY DATE:
January 23, 2013	Renewal Animal Use Protocol	January 31, 2014

Full Board Meeting ☐ AREB Subcommittee ☒ AREB Chair and University Veterinarian ☐ AREB Chair ☐

CERTIFICATION
The University of Saskatchewan Animal Research Ethics Board reviewed the above-named research project. The proposal was found to be acceptable on ethical grounds. The principal investigator has the responsibility for any other administrative or regulatory approvals that may pertain to this research project, and for ensuring that the authorized research is carried out according to the conditions outlined in the original protocol submitted for ethics review. This Certificate of Approval is valid for the above time period.

PROTOCOL MODIFICATIONS
Any modifications to this protocol must be approved by the UCACS AREB Chair prior to implementation, using the AUP Modification Form.

ONGOING REVIEW REQUIREMENTS
Research programs that extend beyond one year must receive annual review. For the annual renewal, an annual review form (and progress report) must be submitted to the AREB within one month of the current expiry date each year the study remains open, and upon study completion. Please refer to the Research Ethics Office website for further instructions.

Michael Corcoran, Chair
Animal Research Ethics Board
University of Saskatchewan

February 11, 2013
Date Issued

Please send all correspondence to:

Research Ethics Office
University of Saskatchewan
Box 5000 RPO University, 1607-110 Gymnasium Place
Saskatoon SK S7N 4J8
Telephone: (306) 966-7928 Fax: (306) 966-2069 Email: ucacs.office@usask.ca

UNIVERSITY OF SASKATCHEWAN

Animal Research Ethics Board (AREB)

Certificate of Approval

PRINCIPAL INVESTIGATOR	DEPARTMENT/ORGANIZATION	ANIMAL USE PROTOCOL #
Dr. David Cooper	Anatomy & Cell Biology	20120112

TITLE
Pilot study to identify bone vascular canals in a rat model using high resolustion imaging.

SPONSORING AGENCIES
Natural Sciences Engineering Research Council (NSERC)

BIOSAFETY NUMBER
ANA-14

UNIFI FUND #

APPROVAL DATE:	APPROVAL OF:	EXPIRY DATE:
January 22, 2013	New Animal Use Protocol	January 31, 2014

Full Board Meeting ☒ AREB Subcommittee ☐ AREB Chair and University Veterinarian ☐ AREB Chair ☐

CERTIFICATION
The University of Saskatchewan Animal Research Ethics Board reviewed the above-named research project. The proposal was found to be acceptable on ethical grounds. The principal investigator has the responsibility for any other administrative or regulatory approvals that may pertain to this research project, and for ensuring that the authorized research is carried out according to the conditions outlined in the original protocol submitted for ethics review. This Certificate of Approval is valid for the above time period.

PROTOCOL MODIFICATIONS
Any modifications to this protocol must be approved by the UCACS AREB Chair prior to implementation, using the AUP Modification Form.

ONGOING REVIEW REQUIREMENTS
Research programs that extend beyond one year must receive annual review. For the annual renewal, an annual review form (and progress report) must be submitted to the AREB within one month of the current expiry date each year the study remains open, and upon study completion. Please refer to the Research Ethics Office website for further instructions.

Michael Corcoran, Chair
Animal Research Ethics Board
University of Saskatchewan

February 7, 2013
Date Issued

Please send all correspondence to:

Research Ethics Office
University of Saskatchewan
Box 5000 RPO University, 1607-110 Gymnasium Place
Saskatoon SK S7N 4J8
Telephone: (306) 966-7928 Fax: (306) 966-2069 Email: ucacs.office@usask.ca

UNIVERSITY OF SASKATCHEWAN

University Committee on Animal Care and Supply (UCACS)
Standard Operating Procedure (SOP)

SOP #	Title
1	Propagation phase contrast micro computed tomography of live rats

1. **Purpose**
   To use synchrotron radiation to image cortical canals in the peripheral limb bones of live * rats using propagation phase contrast x-ray micro computed tomography.

2. **General Information**
   Using phase contrast microCT will allow for the safe in vivo imaging of the network of cortical canals and BMUs which are important in the study of remodelling and bone growth and development.

3. **Equipment/Materials**
   PPE
   Isoflurane anesthesia system (with medical grade oxygen)
   Anesthetic work station (with induction chamber and nose pieces for rats)

4. **Procedure**
   - Animals will be transported from the Animal Facility to the CLS following SOP Z101: Animal Transport and Use of Animals Outside the Animal Facility
   - Live animal imaging will take place with the facility Animal Welfare Veterinarian present.
   - The animal will be transported from the BMIT animal preparation area to the POE-2 hutch in the acrylic induction chamber then anesthetized using isoflurane by inhalation.
   - The animal will then be moved to the CT imaging stage and restrained for safety in a custom designed holder with free air flow where it is immobilized for the entire 10-30 minute scan.
   - Closed circuit cameras will be trained on the animal to monitor breathing and signs of distress. A digital thermostat will maintain ambient room temperature
   - The animal will be scanned under continuous flow of isoflurane/oxygen
   - At the end of the imaging period the mouse will be returned to the acrylic induction chamber and given a lethal overdose of isoflurane for 5 minutes and the animal will be returned to the BMIT animal preparation area.

5. **Safety**
   - PPE

lab coat or gown, gloves, closed toed shoes
- Please read MSDS and ERP regarding proper use of Isoflurane
- Be familiar with proper handling of medical grade oxygen tanks and the operation of -anesthetic machine
- Be familiar with proper animal handling techniques
- Contact the PI or the University Veterinarian for assistance and humanely euthanize if concerns arise.

6. Potential Complications and Troubleshooting

- Beam problems (Short term) during scans at the CLS: keep animal on anesthesia under monitoring until restoration of x-ray flux.
- Beam problems (Long term) during scans at the CLS: Humanely euthanize animal and follow post-scan part of the protocol
- Contact the PI or the University Veterinarian for assistance and humanely euthanize if any welfare concerns arise.

7. References

SOP#2 - K-edge subtraction and computed tomography imaging of live mice.
UCACS Animal Ethics Protocol 20050096 Developing a synchrotron-based imaging protocol for tracking of implanted cells in a living host animal. Val Verge. 2012

Z101: Animal Transport and Use of Animals Outside the Animal Facility

8. Revision History

List the changes made during the most recent revision, as well as the reasons for the changes.

Date Created: Dec 6, 2012		**Written by: Isaac Pratt**
SOP Review and Revision History		
Revision Number	**Revision Date**	**Reviewer**
2	**Dec 16, 2012**	**Dr. David Cooper**